The Electrochemical Society
Advancing solid state & electrochemical science & technology

On The Impact of the Locality on Short-Circuit Characteristics: Experimental Analysis and Multiphysics Simulation of External and Local Short-Circuits Applied to Lithium-Ion Batteries

View the article online for updates and enhancements.

PRIME
PACIFIC RIM MEETING
ON ELECTROCHEMICAL
AND SOLID STATE SCIENCE
2020

Abstract Submission
DEADLINE EXTENDED:
May 29, 2020

Honolulu, HI | October 4-9, 2020

ECS

On The Impact of the Locality on Short-Circuit Characteristics: Experimental Analysis and Multiphysics Simulation of External and Local Short-Circuits Applied to Lithium-Ion Batteries

J. Sturm,[1,z] A. Rheinfeld,[1] D. Buzon,[2,3] and A. Jossen[1,4]

[1]*Institute for Electrical Energy Storage Technology (EES), Technical University of Munich (TUM), 80333 Munich, Germany*
[2]*Univ. Grenoble Alpes, 38000 Grenoble, France*
[3]*CEA, Liten, 38054 Grenoble, France*
[4]*Munich School of Engineering (MSE), Technical University of Munich (TUM), 85748 Garching, Germany*

Emulating true, field-like internal short-circuits (ISCs) by experimental methods is a complex task with mostly unsatisfactory outcome. However, understanding the evolution and impact of ISCs is crucial to mitigate safety issues related to lithium-ion batteries. Local short-circuit (LSC) conditions are applied to single-layered, small-sized (i.e. <60 mAh), and single-side coated graphite/NMC-111 pouch-type cells in a quasi-isothermal test bench using the nail/needle penetration approach. The cell's impedance, capacity, and the contact resistance at the penetration site mainly define the short-circuit current and, hence, the terminal voltage and heat generation rate associated with polarization effects and electrochemical rate limitations, which are correlated to the cell's behavior during external short-circuits (ESCs) at various short-circuit resistances. Measuring the electrical potential between the needle and the cell's negative tab allows to evaluate the polarization across the electrodes and to estimate the short-circuit intensity. LSC simulation studies are used to correlate current flux and resistance to ESC conditions. Double-layered cells are penetrated to create short-circuit conditions within either a single or both electrode stacks to study the difference between multiple LSCs (e.g. during a nail penetration test) and a single LSC (e.g. due to a particle/dendrite). Post-mortem analysis reveals copper dissolution/deposition across both electrodes.

Supplementary material for this article is available online

Recent reports[1] summarizing critical incidents involving lithium-ion batteries (LIBs) revealed similar characteristics of initial over-heating, followed by smoke[2–4] and/or spark emission,[1] and, in case of a self-accelerating heat generation, leading to explosions[5] and/or fire and flames released by the battery.[6,7] Unless the safety of LIBs cannot be maintained under all conditions to minimize or even exclude any harm to the environment/individuals, the current trend toward optimizing cost[8] and performance of LIBs involving higher energy densities[9,10] and/or an improved rate capability[11] may impede the market penetration for mobile, automotive, and stationary energy storage applications.

Safety issues of LIBs can be caused by a variety of internal and external triggers related to manufacturing issues, shortcomings in design, and/or operation strategy,[7] as well as mechanical,[8] electrical, and thermal abuse conditions,[12,13] which can lead to external and internal short-circuit scenarios. Hence, there is a strong need for relevant test scenarios simulating such triggers, which help understanding the underlying mechanisms in order to derive suitable means to mitigate or even rule out safety issues related to LIBs (e.g. shutdown separators,[14] integrated circuits,[15] pyrotechnical safety systems,[16] etc.) by increasing the battery's tolerance toward ESCs and ISCs.

On the one hand, ESC tests revealing a good reproducibility[17] and relevance for simulating realistic high current and abusive short-circuit conditions applied via the terminals of a LIB. On the other hand, simulating ISCs within a LIB by experimental means is a more complex task. As an example for a typical, field-like ISC failure, metallic particle contamination, followed by dissolution and deposition including dendrite growth can lead to a local penetration of the separator and initiate a short-circuit.[18–20] In order to reproduce such a field-like shorting scenario, the test must trigger the shorting only at a single site, set a low ohmic resistance, form over time/operation of the LIB, and should reveal sufficient reproducibility. Adjusting

the locality of the short-circuit seems to be viable regarding the range of already existing test procedures including a complete or partial penetration the LIB with a nail or needle[21] or the insertion of local defects during assembly of the battery,[22] whereas controlling the shorting resistance may only be partly viable due to the variety of possible materials and contact conditions between the electrodes and current collectors[23] as well as possible changes during the shorting scenario.[24] The formation over time can hardly be recreated by experimental methods as the aforementioned defects form over the lifetime of LIBs and exceed practical operation times of safety tests by far. As a result, existing tests such as nail penetration[21,24–29] or the more complex modification of LIB via insertion of local defects in the electrode stack/jelly roll[22,30] cannot satisfactorily simulate a real, field-like ISC scenario but at least approximate similar high current scenarios with a strong local heat generation.

The insertion of local defects such as low-melting temperature alloys[22] require a modification of the electrode stack/jelly roll which may alter the battery's behavior beside time- and cost-intensive efforts to manufacture these prototype cells. In comparison, a nail penetration test can be applied easier using similar cells as used for ESC tests. Investigating both short-circuit conditions applied to the same cells enables for a comparison/correlation to understand the electrical and thermal behavior of locally applied short-circuits.

In sum, so far there is no test that can satisfactorily recreate a realistic, field-like ISC in LIBs. Based on its straightforward applicability, a nail or needle penetration technique was applied to create not field-like ISCs but local short circuits (LSCs) within a cell. In addition to studying the cell's LSC characteristics, ESC tests were applied in accordance with our previous work.[31] The influence of the electrical electrode design was minimized by using the same single-side coated electrodes, with a counter-tab design throughout all tests. By further studying cells with one or two electrode stacks within a quasi-isothermal calorimetric test bench, effects related to the cell's thermal design or the locality of heat generation were minimized. In this work, we investigate the influence of the locality of the shorting scenario via triggering the short-circuit in the center of the electrodes

using the nail/needle penetration technique and eventually compare the cell's local short-circuit characteristics to its external short-circuit behavior. As the external resistance directly correlates to both the current flux and heat generation rate and, hence, defines the intensity of the ESC, a low-ohmic resistance range as expected for the LSC tests was investigated, which enables for a comparison/correlation of the terminal voltage and the heat generation rate in order to evaluate the intensity of the applied LSC scenario. As the locality of the shorting affects local electrode polarization during the LSC tests, a correction of the terminal voltage based on a multi-dimensional simulation study must be applied in order to allow for a direct comparison of LSC and ESC test results, which eventually allows estimating the shorting resistance evoked via nail/needle penetration. Using the quasi-isothermal, calorimetric test bench, the short-circuit proceeds without triggering a high local heat generation rate, which may lead to thermal, self-accelerating processes such as a thermal runaway scenario. Usually, this applies when local particle insertion procedure or nail penetration tests are applied for emulating ISC scenarios in LIBs. By applying our technique, we can mitigate the influence of these thermal effects and study the pure electrical short-circuit behavior at the beginning of the short-circuit (i.e. <1 s) and the subsequent, various electrochemical rate limitation effects (i.e. >1 s),[31,32] which are caused by either the anode or the cathode within the tested cells. To further study various LSC conditions in a stacked electrode configuration, nail/needle penetration were further applied to cells with two electrode stacks with and without a hole within one of the electrode stacks. This allows for applying either a LSC across both electrode stacks representing a complete penetration during a common nail penetration test or a LSC within only one of the two electrode stacks representing a local piercing of a separator such as occurring within the final stage of an ISC. Various diameters of the needle were used during the penetration resulting in differently sized penetration sites and consequently, different short-circuit resistances. To increase the understanding of the electrical and thermal behavior during the ESC and LSC scenario, the characteristic current, electrical potential and heat rate signals of all tests are analyzed toward significant plateau and transitionzones[31,33] referring to the cell's polarization and rate limiting electrochemical processes within the electrodes. The observed overdischarge occurring during all tests can be correlated to severe copper dissolution of the negative current collector including copper deposition throughout and across both electrodes using *post-mortem* analysis.

Experimental

Calorimetric test bench for short-circuit tests.—The calorimetric setup for the ESC and LSC test is schematically shown in Fig. 1. In our previous work, the test bench was used for applying ESC tests[31] and is modified in this work for applying LSC tests (i.e. nail/needle penetration tests) as well. For the potentiostatic measurements of current flux and electrical potential, a potentiostat (SP-300, Bio-Logic Science Instruments) and a source measurement unit (SMU, B2901A, Keysight Technologies) were used. In terms of ESC tests, a 10 A/5 V amplifier (SP-300, Bio-Logic Science Instruments) extends the current range to apply the expected current peaks around 10 A in the very beginning of the short-circuit. Besides applying a 0 V condition at the cell's terminals via the potentiostat, an external resistance (i.e. 5, 50, and 500 mΩ) was used to vary the intensity of the ESC condition[31,33] as depicted in Fig. 1 (left) whereas the SMU measures the cell's voltage (E_{sc}) at the cell's terminals. The current flux at the tabs (I_{sc}) can only be measured in case of ESC tests, and not for the LSC tests. Regarding the LSC tests, only the terminal voltage is measured via the potentiostat without the amplifier. The SMU is used to measure the electrical potential (Φ_{sc}) at the penetration site in the center of the active electrode area (i.e. needle) vs the cell's negative tab (see Fig. 1, right). The stainless steel needles (2R2, Unimed) are electrically connected to measure the expected potential drop across the electrodes because of the current flux, geometrical configuration, and contact resistance, and may be correlated to the polarization of the cell. For the

calorimetric measurement, three digital multimeters (DMM, 34 470A, Keysight Technologies) measure the cell's temperature at the positive current collector tab/terminal (T_{tab}), the bottom ($T_{cu,1}$), and the upper ($T_{cu,2}$) copper bar ($45 \times 45 \times 90$ mm, CW004A) which mechanically clamp the tested cell. The clamping pressure is expected not to distort the electrical-thermal behavior of the cell. The temperature signals during ESC and LSC tests are used to calculate the heat generation rate from the short-circuit scenario. The upper and bottom copper bar exhibit a narrow through-hole and a shallow-hole for the penetration needle, which requires a new calibration similarly to our previous work.[31] Pt100 sensors at an accuracy of ± 0.15 C at 0 C (DIN/IEC Class A) centrally measure the temperature of the copper bars (installed with a thermal adhesive). To reduce the thermal contact resistance between the copper bars and the cell, ceramic foils (86/600 Softtherm, Kerafol Keramische FolienGmbH) of 0.5 mm thickness and 6 W m^{-1} K^{-1} were used at the interface as shown in Fig. 1. The measurement device is embedded in a 12 cm extruded polystyrene foam (XPS) at a thermal conductivity of 0.04 W m^{-1} K^{-1} to impede the heat exchange to the surrounding climate chamber. The whole setup is placed in a custom built climate chamber[34] incorporating resistive heating and Peltier-cooling to set the ambient temperature to 25 C. Reference measurements with a thermometer (1524, Fluke Corporation) revealed a temperature accuracy of ± 0.03 C.

As shown in Fig. 1, the LSC is triggered via rotation of the short-circuit device (1) formed of a an indexing plunger[35] with a plastic rod attachment (PEEK) which incorporates the needle, subsequent forward movement (2) via a linear spring of $\triangle x = 9.7$ mm displacement at a spring rate of 7.861 N mm^{-1} ($1 \times 6 \times 18$ mm, Febrotec), and finally penetration (3) of the tested cell with the needle.

In sum, the adaption of the calorimetric test bench incorporated the insertion of the short-circuit device to apply the nail penetration for the LSC test and the adjustment of the copper bars, which requires a re-calibration of the setup.
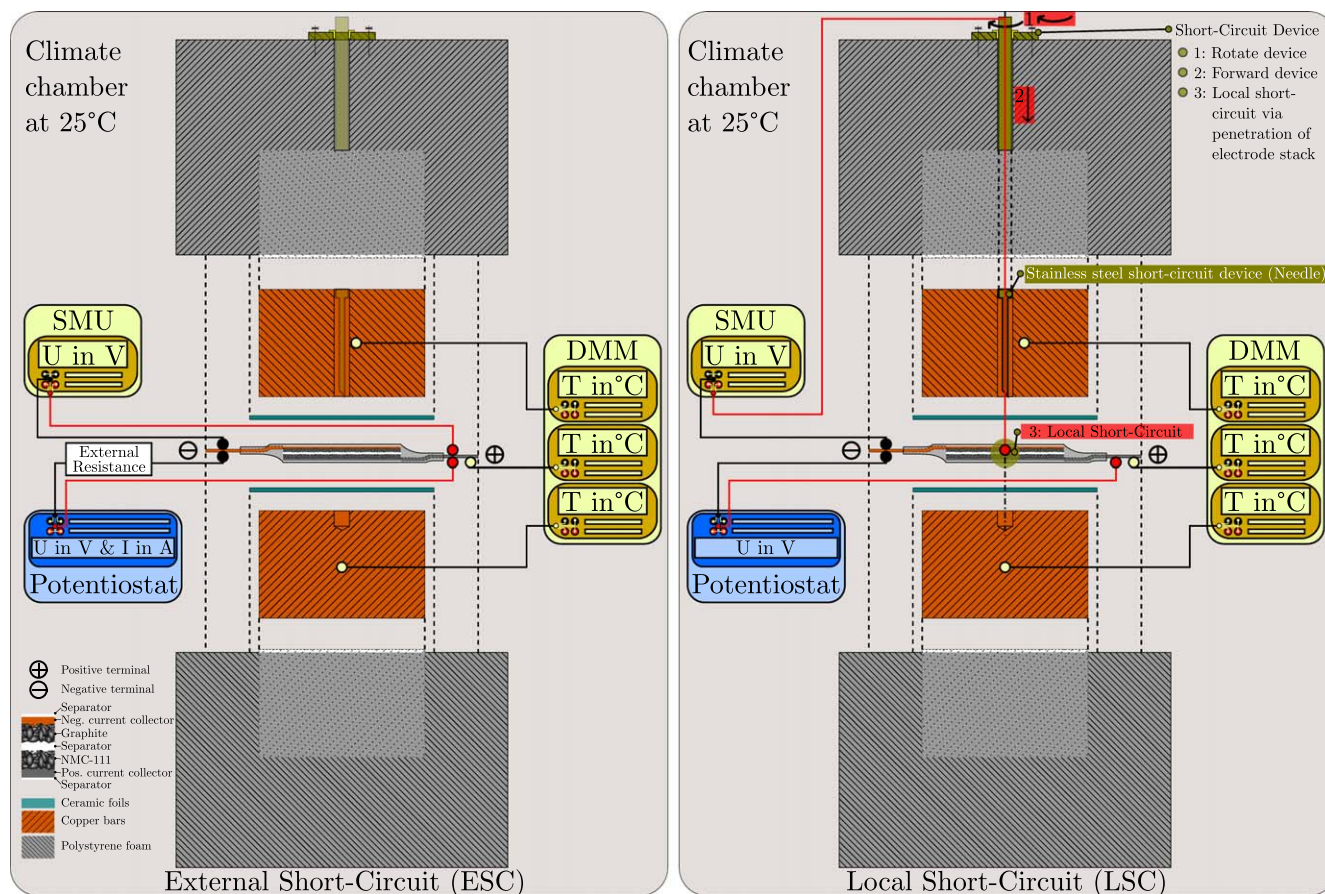
Calibration of the calorimetric test bench.—The calibration procedure is used for the temperature sensors, the determination of heat capacities, and losses to the environment. The calibration of the three Pt100 sensors uses a reference thermometer (1524, Fluke Corporation) equipped with a platinum resistance thermometer (5662, Fluke Corporation).[31] To determine the calorimetric constant (i.e. heat capacity and losses to the environment), a single-layered pouch-type cell (i.e. calibration cell)[31] similar to the cells of this work is equipped with two resistive heaters connected in series (1218.4 Ω, Thermo Technologies) and using the SMU, three different heat rates (0.1, 5, and 10 W) were applied for different durations (7200, 144, and 72 s) resulting in an overall applied amount of heat around 720 J. The measured temperature increase of the two copper bars $\left(\frac{d\bar{T}_{cu,i}}{dt}\right)$ and the calibration cell $\left(\frac{d\bar{T}_c}{dt}\right)$ multiplied with their heat capacities ($C_{p,i}$) can be correlated to the applied heat rate ($\dot{Q}_{tot}^*$) whilst accounting for heat exchange ($\alpha_{cu,i}$) of the copper bars to the climate chamber (T_∞) as follows[31]:

$$\dot{Q}_{tot}^* = C_{p,1}\frac{d\bar{T}_{cu,1}}{dt} + C_{p,2}\frac{d\bar{T}_{cu,2}}{dt} + C_{p,c}\frac{d\bar{T}_c}{dt}$$
$$+ \alpha_{cu,1}(\bar{T}_{cu,1} - T_\infty) + \alpha_{cu,2}(\bar{T}_{cu,2} - T_\infty) \quad [1]$$

Correcting the measured copper temperatures with the heat losses to the ambience, the adiabatic temperatures ($\bar{T}_{ad,i}$) of the copper bars and the measured cell temperature ($\bar{T}_c$) are used together with applying an iterative linear fit[31] of their effective heat capacities ($C_{p,i}$) to fit the applied heat rate as[31]:

$$\dot{Q}_{tot}^* = C_{p,1}\frac{d\bar{T}_{ad,1}}{dt} + C_{p,2}\frac{d\bar{T}_{ad,2}}{dt} + C_{p,c}\frac{d\bar{T}_c}{dt} \quad [2]$$

Finally, the thermal inertia of the test bench must be considered to derive the total heat rate ($\dot{Q}_{tot}$) and dissipated heat (Q_{tot}) via

Figure 1. Schematic view of the calorimetric test bench for ESC (left) and LSC (right) tests applied to the pouch-type cells depicted in the center of each configuration. The test bench is placed inside of a climate chamber at 25 °C and the potentiostatic (Potentistat, SMU) and calorimetric (DMM) measurement devices are depicted with their respective sensor locations. For the LSC tests, the penetration procedure (see steps 1, 2, and 3) using the short-circuit device with the penetration needle is shown in the upper right part.

accounting for a certain time lag ($\triangle t_\infty$) and an approximately linear[31] heat offset ($\triangle Q_\infty$) as:

$$Q_{tot} = Q_{tot} + \triangle t_\infty \cdot \dot{Q}_{tot} \cdot \left(1 - \exp\left(-\frac{t}{\triangle t_\infty}\right)\right)$$

$$\dot{Q}_{tot} = \dot{Q}_{tot}\left(1 + \exp\left(-\frac{t}{\triangle t_\infty}\right)\right) \qquad [3]$$

A more detailed description of the calibration and the processing of the measured data is given in the supplementary material of this work at (stacks.iop.org/JES/167/090521/mmedia).

The heat capacities ($C_{p,i}$) are calculated to 660.6 J K^{-1} (407.8 J kg^{-1} K^{-1}) and 659.8 J K^{-1} (407.2 J kg^{-1} K^{-1}) for the bottom and the upper copper bar. The heat capacity of the pouch-type cell ($C_{p,c}$) is iteratively determined to approximately 900 J kg^{-1} K^{-1} (5.9 J kg^{-1} K^{-1}), which is well in line with comparable pouch-type cells.[36,37] The time lag ($\triangle t_\infty$) accounts to 5.9 s and the linearized heat offset ($\triangle Q_\infty$) is depicted in the supplementary material.

To conclude, the modification of the calorimetric test bench for LSC tests reveal a shorter time lag due to shorter maintenance intervals for the ceramic foils and slightly increased mechanical clamping, and comparable calorimetric constants as shown in our previous work.[31]

Pouch-type lithium ion cells for short-circuit tests.—19 custom built (Custom Cells Itzehoe GmbH), pouch-type LIBs were investigated under quasi-isothermal external (4 cells) and local (15 cells)

short-circuit conditions. The four different pouch-type LIBs (i.e. configuration P1, P2, P3, and P4) studied within this work mainly differ in their stacking sequence of electrode and separator layers which is schematically shown in Fig. 2. The stacking sequence of separator (SEP), graphite anode (A) and NMC-111 cathode (C) from configuration P1 to P4 are as follows:

- **P1**: SEP/A/SEP/C/SEP
- **P2**: SEP/A/SEP/C/SEP/C/SEP/A/SEP
- **P3**: SEP/A*/SEP/C*/SEP/C/SEP/A/SEP
- **P4**: SEP/C*/SEP/A*/SEP/A/SEP/C/SEP

A polyolefin separator (SEP) of 20 μm electronically insulates the electrode pairs and is wrapped around the entire electrode stack to ensure its position. 1 M of LiPF$_6$ solved with ethylene carbonate (EC) and dimethyl carbonate (DMC) at a weight ratio of 1:1 and 2 wt% vinylene carbonate (VC) was used as electrolyte. Configuration P2 (double-layered) differs from P1 (single-layered) only in the total number of electrode pair. Configuration P3 (double-layered) differs from P2 as the upper electrode pair (see Fig. 2) includes a centered hole ($\oslash$ 5 mm) through the anode (A*) and the cathode (C*) to enable penetration only in the bottom stack in order to initiate an LSC, which subsequently applies an ESC in the upper stack via the current collector paths. Configuration P4 (double-layered) differs from P3 only in the sequence of the layers as the anodes are facing each other in the middle part to investigate if the sequence of electrode penetration influences the short-circuit behavior in terms of varying shorting resistances. All electrodes were single-side coated to guarantee comparability between the resulting cell polarization in the ESC and LSC tests.
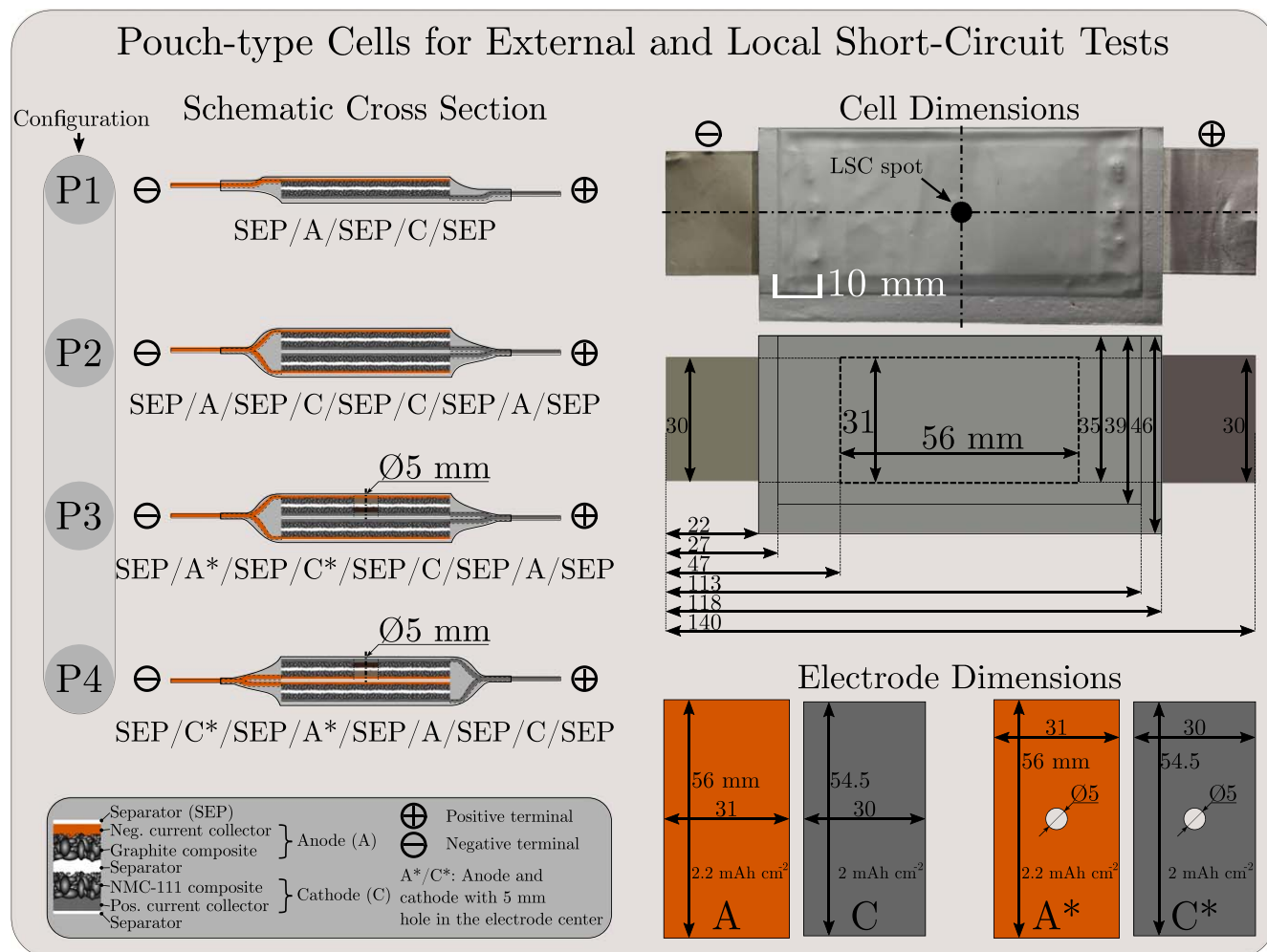
Figure 2. Schematic cross-section of the single- (i.e. P1-type) and double-layered (i.e. P2-, P3-, and P4-type) pouch-type LIBs showing the electrode and separator stacking sequence (left). Despite various stacking sequence chosen for the configuration P3 and P4, the main difference to P2 is that the upper electrode pair comprises a 5 mm hole to enable LSC tests based on the penetration of only one electrode stack (see "Electrode Dimensions"). The geometrical size of the test cells is depicted under "Cell Dimensions" with the centered position for the nail penetration site used for the LSC test.

All tests carried out in this work are summarized in Table I showing the initial cell voltage, state of charge (SoC), initial cell temperature/ambient temperature (T_∞), and the shorting condition for the ESC (0 V as well as 5, 50, and 500 mΩ, Power Metal Strip, Vishay Intertechnology Inc.) and the LSC tests with varying nail/needle diameters ($\oslash d$ of 0.5, 1, and 2 mm, 2R2, Unimed), respectively.

In order to determine the balancing and analyze the expected overdischarge,[31] differential voltage analysis (DVA) was applied to cell P2#10 and self-built CR2032-type half cells of pristine anode and cathode samples ($\oslash$ 14 mm, Custom Cells Itzehoe GmbH) vs lithium metal ($\oslash$ 15.6 mm $\times$ 250 μm, MTI Corporation). Based on the supplier's information and our measurements, 96 wt.-% of graphite combined with each 2 wt.-% of binder and conductive carbon form the anode composite at a final thickness of 67 μm on a 12 μm copper foil which results in an areal capacity of 2.2 mAh cm^{-2} and a gravimetric loading of 350 mAh g^{-1}. The cathode contains 86 wt.-% of NMC-111 (i.e. equal proportion of nickel, manganese, and cobalt) combined with 6 wt.-% of binder and 8 wt.-% conductive carbon at 79 μm on a 18 μm aluminum foil which results in an areal capacity of 2 mAh cm^{-2} (145 mAh g^{-1}). For the DVA, the full cell (P2#10) was charged and discharged at a constant current (CC) at 600 μA ($\approx$0.01 C) using a battery cycler (CTS, Basytec GmbH) in a climate chamber (VT 4021, Vötsch Industrietechnik GmbH) at 25 C. The half cells were assembled in an argon-filled glove box (H$_2$O, O$_2$ < 0.1 ppm,

M.Braun Inertgas-Systeme GmbH) using two glassfiber separators ($\oslash$16 mm $\times$ 250 μm), two stainless steel spacers ($\oslash$16 mm $\times$ 0.5 and 1 mm), the CR2032-type housing caps, wave spring, insulation ring and 90 μl of 1 M of LiPF$_6$ EC:DMC (1:1 by weight) and 2 wt.-% VC. Formation of the coin cells included an initial 33.9/30.7 μA ($\approx$0.01 C) lithiation from 2.789/3.172 V to 10 mV/3 V and 6 subsequent cycles at 30 μA CC charge and discharge (between 1.7 V and 10 mV/3 V and 4.3 V) with constant voltage (CV) periods until $\pm$6.8/6.1 μA for the anode and cathode half cell with the same measurement equipment. Finally an anodic delithiation and cathodic lithiation profile was used after stable capacity retention appeared (<0.01 %).

In sum, LSC tests were applied to the P1-type cells to correlate the electrical-thermal characteristics to the P1-type ESCs at various external resistances. The set of experiments proposed on single-layered ("P1-LSC") and double-layered cells ("P2-LSC" and "P3/P4 —coupled LSC/ESC") give the opportunity to investigate and decouple the different phenomena occurring in a stacked, pouch-type LIB during LSC tests.

Measurement procedure for ESC and LSC tests.—Table II shows the procedure for the ESC and LSC test, starting with "Initial cycles" using a battery cycler (CTS, Basytec GmbH) and a climate chamber at 25 C (KT115, Binder) to exclude any influence of formation processes. Pulse measurements at 50% SoC were applied to characterize the dynamic electrical behavior at different C-rates.

Table I. Overview of ESC and LSC Tests Applied to the Studied Cells.

Scenario	$E_{sc,0}$/V	SoC_0/—	T_∞/K	R_{ext}/mΩ
ESC tests				
P1#5[b]	4.2 V	100%	25 °C	0 ($\equiv$"0 V")
P1#10[b]				5
P1#6[b]				50
P1#7[b]				500
LSC tests				$\oslash d_{Needle}$
P1—LSC				
P1#2[b]	4.2 V	100%	25 °C	1 mm
P1#3[b]				
P1#9				
P2—LSC				
P2#1[b]	4.2 V	100%	25 °C	1 mm
P2#10[a]				
P3/P4—coupled LSC/ESC				
P3#1	4.2 V	100%	25 °C	1 mm
P3#2				
P3#4[b]				
P4#1[b]				
P4#2				
Varying needle diameter				
P2#3	4.2 V	100%	25 °C	2 mm
P2#4				
P2#5	4.2 V	100%	25°C	0.5 mm
P2#6				
P2#7				

a) Used for DVA. b) Used for *post-mortem* analysis.

A single "Capacity check-up" was used to determine the initial capacity (C_0) at 0.5 C CC discharge from 4.2 to 3 V and in the subsequent "Preconditioning" 0.2 C CC charge with a CV period until 0.01 C prepares the cells at 4.2 V (=100% SoC). Afterwards, the cells were embedded in the calorimetric test bench (see Fig. 1), electrochemical impedance spectroscopy (EIS, see Table II) determined the cell's impedance ($R_{i,0}$) and the setup was rested for 12 h to allow for thermal equalization.

The "Quasi-isothermal short-circuit scenarios at 25° C" initiates after a resting period and subsequently differs for the ESC and LSC tests in terms of the potensiostatic sampling (see Table II). In case of the ESC, a constant voltage phase (4.2 V) to precondition the measurement device is applied and after 5 s, a 0 V condition is set in reference to the cell's terminals. The sampling rate is subsequently reduced to sufficiently but not excessively record the dynamic behavior and limit memory allocation. The ESC is terminated, when the current measured by the potentiostat falls below 100 μA and finally a resting phase of 17 h records relaxation. In case of the LSC, the short-circuit device is triggered right after the resting period (10 s) and the sampling rates are continually reduced as well. The cells tested in the LSC tests are exposed to a longer discharge than those tested in the ESC tests as the LSC test was terminated after $\approx$20 h. Simultaneously to the potentiosatic measurements, the calorimetric measurement includes the temperatures of the cell and the upper/bottom copper bar. Finally, EIS was applied to determine the cell's impedance ($R_{i,sc}$) and the terminal voltage ($E_{sc,end}$) after the short-circuit event.

As possible investigations toward the influence of initial state of charge and ambient temperature have been thoroughly discussed for ESCs,[31] similar influences are expected for the studied LSCs and the tests are consequently carried out at 100% SoC and 25 C without exception.

Correlation of ESC and LSC tests.—Local variations in electrode polarization (i.e. along the electrodes' thicknesses, widths, and lengths) are expected between the external and the local short-circuit scenario and, hence, different spatial distribution of the current flux. Assuming the same shorting current (i.e. the same shorting intensity) from an ESC and LSC test applied to identical cells, a certain offset of the resulting terminal voltages can be expected simply due to the spatial distribution of current flux. To correlate the resulting terminal voltages from the ESC and the LSC tests, the local variations of the electrode polarization should be considered. Therefore, multidimensional multiphysics simulation studies investigate exemplary ESC and LSC scenarios for the P1-type cells corresponding to an ESC test at an external short-circuit resistance of 243.9 mΩ, which lies in the range of the cells' initial impedances. The simulative work is outlined in the supplementary material as it exceeds the experimental focus of this work. Both short-circuit simulations reveal nearly the same shorting current over time whilst the local polarization effects (i.e. along the electrodes' thicknesses, widths, and lengths) reveal significantly differing local current flux and potential distribution. As a result, the offset between the terminal voltages is calculated and normalized with respect to the ESC results. Extrapolation from the external short-circuit resistance applied in the ESC case, reveals a high prediction accuracy of the local short-circuit resistance with errors below 2% until 100 ms.

Regarding the measured terminal voltages from the P1-LSC cells, a simulation-derived correction factor of 0.062 at 100 ms was used in this work to account for the aforementioned local polarization effects and enable for the comparison to the P1-type ESC test results. The corresponding external resistance for the shorting scenario can be calculated for the LSC tests, which must have been applied to gain the same current flux/shorting intensity resulting from a P1-type ESC test. The calculation itself uses the electrical potential difference to the P1-type ESC results showing a higher (i.e. 50 mΩ ESC test) and a lower terminal voltage (i.e. 5 mΩ ESC test) at 100 ms. By further interpolating the calculated effective external short-circuit resistances, the short-circuit resistance of the LSC tests can be estimated.

Post-mortem analysis.—*Post-mortem* analysis is used to qualitatively study effects such as active material degradation and/or copper dissolution/deposition occurring during the short-circuit tests. The cells were opened in an argon-filled glove box (H$_2$O, O$_2$ < 0.1 ppm, M.Braun Inertgas-Systeme GmbH) for a first visual inspection and $\oslash$ 14 mm samples were subsequently extracted for scanning electrode microscopy (SEM) and energy-dispersive X-ray spectroscopy (EDX) measurements. The samples were washed with diethyl carbonate (DEC) and dried before applying SEM/EDX (JCM-600, JEOL Ltd.) where a MP-00040EDAP detector at 15 kV acceleration voltage offered magnifications levels from 150 to 2000 of the electrodes.

Results and Discussion

Beginning with the DVA analysis, Fig. 3a shows the open circuit potentials (OCPs) of the coin cells together with their superposition ("Graphite + NMC-111 coin cells") as a function of full cell SoC (i.e. P2#10). The superposition reveals marginal errors (see Fig. 3b) around 10 mV with increased deviations at low SoCs due to the steep rise of the anode potential at low lithiation levels. The overcharge and overdischarge zone are depicted beyond the safe operation window between 0 to 100% SoC referring to 3 and 4.2 V. Regarding the 1st derivative in Fig. 3c, the balancing of the anode and cathode in reference to the full cell is shown with similar deviations. The ESC and LSC tests considerable result in an overdischarge of the tested cells, which most likely provokes side reactions besides a highly delithiated anode and a highly lithiated cathode. In this context, the differential capacities are shown in Figs. 3d and 3e, where the capacity gain from de-/intercalation reaction during overdischarge approaches zero. As a result, the overdischarged capacity may not be related to de-/intercalation reaction within the active materials but most likely to side reactions such as copper dissolution/deposition occurring at $\gtrsim$3.2 V vs

Table II. Test Procedures

Initial cycles

Repetition	Sequence[a]	Feature	Chamber Temperature
2×	CC$_{CH}$-CV-R-CC$_{DCH}$-R	CC: 0.1 C, 3 V–4.2 V CV: <0.01 C R: 15 min	25°C
8×	CC$_{CH}$-CV-R-CC$_{DCH}$-CV-R	CC: 0.5 C, 3 V–4.2 V CV: < ± 0.01 C R: 15 min	
1×	CC$_{CH}$-R	CC: 0.5 C to 50% SoC R: 30 min	
1×	P$_{CH}$-R-P$_{DCH}$-R	P: 0.3, 1 and 2 C for 10 s R: 10 min	

Capacity check-up

1×	CC$_{CH}$-CV-R-CC$_{DCH}$-R	CC: 0.5 C, 3 V–4.2 V CV: <0.01 C R: 15 min	25° C

Preconditioning

1×	CC$_{CH}$-CV-R	CC: 0.2 C, 3 V–4.2 V CV: <0.01 C R: 2 h	25° C

EIS at 4.2 V with 1 mA excitation current from 100 mHz to 10 kHz[b]

Quasi-Isothermal short-circuit scenarios at 25 °C

Termination and measurement conditions of the calorimetric test bench (see Fig. 1)

Resting for 12 h

Potentiostatic duration phase and measurement sampling frequency

	ESC		**LSC**	
R	10 s at 1 Hz			
CV	5 s at 10 Hz	R		10 s at 1 Hz
ESC	10 s at 10 kHz	**LSC**		30 s at 10 kHz
	100 s at 100 Hz			120 s at 100 Hz
	$I_{sc} < 0.1$ mA at 10 Hz			20 h at 10 Hz
R	17 h at 1 Hz			

Calorimetric duration phase and measurement sampling frequency

20 s at 1 kHz
100 s at 100 Hz
880 s at 10 Hz
150 min at 1 Hz
until end at 0.5 Hz

EIS with 1 mA excitation current from 100 mHz to 10 kHz[b]

a) CC$_{CH}$ constant current charge CC$_{DCH}$ constant current discharge CV constant voltage R rest/relaxation period P$_{CH}$ charge pulse current P$_{DCH}$ discharge pulse current. b) 6 points per decade and 2 measurements per frequency.

Li/Li$^+$.[38] The ESC and LSC test conditions lead to high anodic overpotentials (>1.6 V)[31] and together with the low lithiation stages in the graphite anode resulting in potentials >1.7 V vs Li/Li$^+$ (see Fig. 3a), oxidation of the copper current collector is most likely triggered, which is indicated here via DVA analysis and will be verified in the *post-mortem* section. Table III summarizes the potentiostatic measurement data for all cells studied by means of ESC and LSC tests. The initial (C_0) and overdischarged (C_{sc}) capacity is only shown in case of the ESC tests via the current flux measurement and the cells are overdischarged $\left(\frac{C_{sc} - C_0}{C_0}\right)$ to 34.9, 28.6, 30.8, and 26.1% for the 0 V, 5, 50, and 500 mΩ condition. Regarding the cell's impedance increase $\left(1 + \frac{R_{i,sc} - R_{i,0}}{R_{i,0}}\right)$, manufacturing tolerances of the tested cells most likely cause the various initial impedances and capacities. The resulting overdischarge, impedance rise and maximum current peak are hereby affected. Similar variations of the initial capacity and the impedance appear for the cells applied with the LSC tests. Additionally, the various contact conditions[23] at the penetration site may affect the resulting impedance increase and the final terminal voltage. Maximum impedance increases by a factor of 1.98, 1.64, 1.72, and 1.53 appear

for the P1-LSC, P2-LSC, P3/P4-coupled LSC/ESC and the varying needle diameter LSC tests, which are in the range of the ESC test results. After the end of each test, the higher terminal voltages of the ESC tests ($E_{sc,end} > 800$ mV, see Table III) are caused by the aforementioned shorter short-circuit exposure compared to the LSC tests, which is also reflected in a lower, local copper deposition across the electrodes shown in the *post-mortem* part (see *Post-mortem* analysis).

Potentiostatic correlation of ESC and LSC tests.—The difference in applying the ESC conditions compared to the LSC using nail penetration raises the question, if and to which extent the resulting electrical and thermal behavior differs and how the intensity of the shorting scenario (i.e. hard or soft) can be compared/correlated from the resulting current flux, potential, and temperature measurements. Evaluation toward various ESC tests, which vary in their intensity and the appearing onset of electrochemical limitation mechanisms caused by the applied external condition (i.e. 0 V as well as 5, 50, and 500 mΩ), are using the terminal voltage for a first, simple correlation as the current flux is not measureable for the LSC tests. As shown in our previous works[31,32] investigating P1-type ESC tests, the cell's polarization correlates to the electrochemical
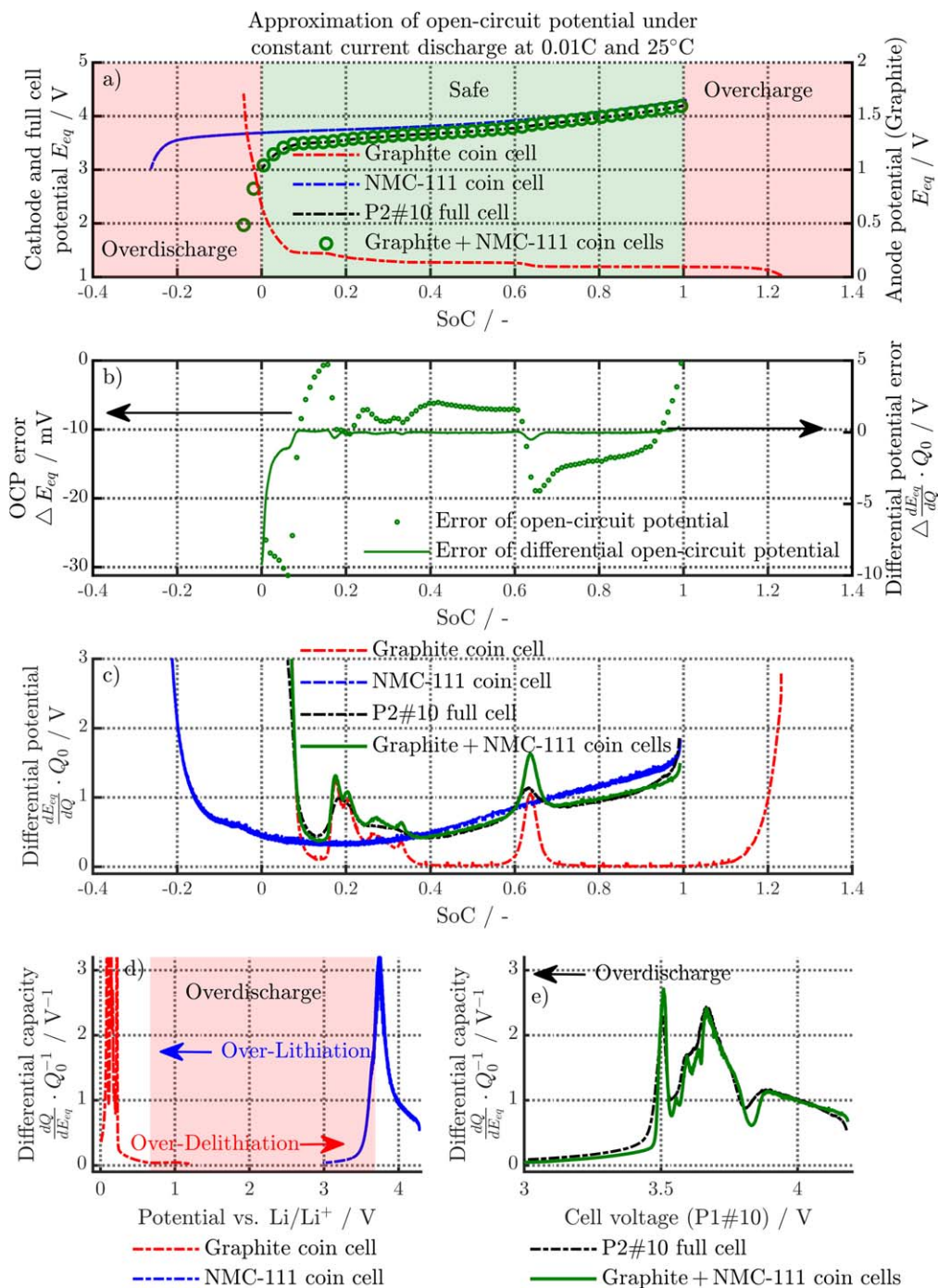
Figure 3. DVA using the measured potentials of full (double-layered pouch-type cell "P2#10") and half cells ("Graphite coin cell" and "NMC-111 coin cell") vs lithium metal and its superposition ("Graphite + NMC-111 coin cells") under OCP CC discharge (≈0.01 C) conditions. Subplot a) shows the measured and calculated potentials and subplot c) shows the corresponding 1st derivative. The calculated superposition of both half cells is compared to the full cell in both cases showing the resulting errors in subplot b). Subplot d) and e) show the differential capacity of the half (d) and full cell (e) together with the superposition to emphasize the potentials vs Li/Li⁺, the terminal voltage and the marginal capacity gain during overdischarge from the de-/intercalation reaction.

limitations and the resulting plateau/transition zones of the current flux, terminal voltage, and heat generation rate can be interpreted as follows:

- **Plateau zone I**: Polarization dominated by ohmic losses in the electrolyte throughout the entire electrode stack and most likely limiting delithiation kinetics in the graphite electrode
- **Transition zone I-II**: Increasing polarization due to liquid phase depletion within the cathode and possible solid phase depletion within the anode leading to current and electrical potential drop

- **Plateau zone II**: Second plateau zone with solid (i.e. saturation of Li-ions due to solid-phase diffusion limitation near the separator) and liquid (i.e. depletion of Li-ions in the electrolyte near the current collector) mass transport limitations at the cathode surface throughout the entire electrode (stage "a") followed by a saturation at the cathode particle (stage "b")
- **Transition zone II-III**: Depletion of anode particles' surfaces lead to polarization increase with further current and potential drop, as well as possible copper dissolution/deposition from the negative current collector

Table III. Potentiostatic Results of ESC and LSC Tests Applied to the Studied Cells.

Scenario	C_0/mAh	C_{sc}/mAh	$R_{i,0}$/mΩ	$R_{i,sc}$/mΩ	$1 + \frac{R_{i,sc} - R_{i,0}}{R_{i,0}}$/—	$E_{sc,end}$/V	I_{max}/A	R_{ext}/mΩ
ESC tests								
P1#5[b]	23.3	35.8	214.7	372.2	1.73	0.810	9.9496	0 (i.e. "0 V")
P1#10[b]	25.6	35.9	226.6	517.7	2.28	0.864	10.0822	5
P1#6[b]	24.5	35.4	207.1	376.9	1.82	0.800	9.2152	50
P1#7[b]	26.9	36.4	201.4	309.0	1.53	0.854	4.9635	500
LSC tests								$\oslash d_{Needle}$
P1—LSC								
P1#2[b]	17.1	n.a.	359.7	587.8	1.63	0.038	n.a.	1 mm
P1#3[b]	19.1		357.4	547.8	1.53	0.074		
P1#9	28.2		298.7	592.4	1.98	0.234		
P2—LSC								
P2#1[b]	59.9	n.a.	222.6	365.4	1.64	0.061	n.a.	1 mm
P2#10[a]	49.9		276.7	418.6	1.51	0.005		
P3/P4—coupled LSC/ESC								
P3#1	53.2	n.a.	285.5	428.4	1.50	0.020	n.a.	1 mm
P3#2	55.5		277.9	480.5	1.72	0.590		
P3#4[b]	57.9		236.7	384.2	1.62	0.149		
P4#1[b]	49.6		242.2	357.2	1.47	0.043		
P4#2	52.4		257.9	423.7	1.64	0.026		
Varying needle diameter								
P2#3	50.6	n.a.	289.6	443.2	1.53	0.276	n.a.	2 mm
P2#4	45.5		307	468.9	1.52	0.581		
P2#5	51.9	n.a.	397.5	560	1.40	0.022	n.a.	0.5 mm
P2#6	50		285.4	407.6	1.42	0.057		
P2#7	51.4		292	412.9	1.41	0.009		

a) Used for DVA. b) Used for *post-mortem* analysis.

• **Plateau zone III**: Continuing de-/intercalation and copper dissolution/deposition with attenuation of the overall physical processes

Analyzing the current flux and terminal voltage profiles of the P1-type ESC tests of this work, similar zones appear as shown in Figs. 4a and 4b. Table IV summarizes the test duration until each plateau and transition zone ends (i.e. t_{end}).

High current rates appear during stage I (see Figs. 4a and 4b) starting at 9.95 ($\approx$427 C), 10.1 (394 C), 9.2 (376 C), and 4.96 A (185 C) for the 0 V, 5, 50, and 500 mΩ condition, respectively. Subplot b magnifies the transition zone I-II and illustrates the higher the external resistance, the later the transition begins and the softer the short-circuit becomes. Zone II reaches around 10 C in all cases. The transition of zone II a and II b appears similarly around 73 s for all ESC tests. Beyond 500 s, zone III initiates and lasts until the end of the test (i.e. $I_{sc} < 0.1$ mA). For the 0 V and 5 mΩ ESC test, control limitations of the measurement equipment cause the observed fluctuations between 20 and 200 ms.

Regarding the terminal voltage in Fig. 4c, the different stages appear similarly for the P1-LSC results. The terminal voltages lie in between the 5 and 50 mΩ ESC test and the zones I, I-II, and II can be determined as shown in Table IV. Comparing the ESC and LSC results in the very beginning of the short-circuit (i.e. zone I, <3 ms), the lowest voltage values appear for the LSC cases which indicate a very high intensity or a so called hard short. As soon as electrochemical rate limitation effects initiate (i.e. zone I-II), the electrical behavior shows subsequently (i.e. zones I-II to III) similar damping/attenuation characteristics as the ESC cases. To conclude, the locality of the short-circuit defines the electrical behavior in the very beginning (i.e. <1 s, zone I), but the subsequent electrical short-circuit behavior is similar to the ESC scenarios and is mainly defined by electrochemical rate limitation effects. Regarding the comparison of the terminal voltages in Fig. 4c, one could simply estimate the intensity of the LSC tests in between the 5 and 50 mΩ ESC test. The noisy signals appearing for the LSC cases are most likely caused via

marginal mechanical oscillation by the shorting device in stage I and caused by the measurement equipment in the following zones.

Figure 4d is used to compare the terminal voltage (E_{sc}) to the electrical potential measured between the cell's negative tab and the needle (Φ_{sc}) in order to evaluate the local polarization effects during the P1-LSC tests. The locally measured potentials show a higher ohmic drop just at the beginning and proceed similarly to the tab potential at lower electrical potentials. Comparing the P1-LSC tests, the P1#3 tests shows a higher potential offset to the terminal voltage as the P1#2 test. As the cell's initial impedances are approximately the same (see Table III), a lower ohmic resistance in the penetration site is expected resulting in the overall lower electrical potentials and the higher spread between them. A certain measurement fuzziness is expected such as the contact condition[23] may change in the penetration site, the ohmic drop due to the current flux through the needle, and the polarization along the negative current collector. Nevertheless, the measured lower potentials at the penetration site indicate that the locality of the LSC (i.e. short-circuit in the center of the electrode stack) complicates the correlation to ESC tests when the measured terminal voltages are compared. As a result, simply correlating ESC and LSC via the terminal voltages as mentioned before may incorporate a certain error due to the different polarization effects across the electrodes caused by the ESC and LSC condition. In the following part, simulation studies help to evaluate the electrical potential fields across the electrodes for P1-type ESC and P1-LSC tests, which simulate the same current flux during the shorting scenario. The correlation uses the resulting terminal voltage difference and the derived correction factor is applied to the measured terminal voltages of the P1-LSC tests in order to estimate the current flux and shorting resistance by interpolating between the P1-type ESC results.

Correction of LSC polarization effects.—As discussed before, comparing the terminal voltages may incorporate a certain error due to the expected high local polarization around the penetration site in the LSC tests as indicated by the local potential measurements (see
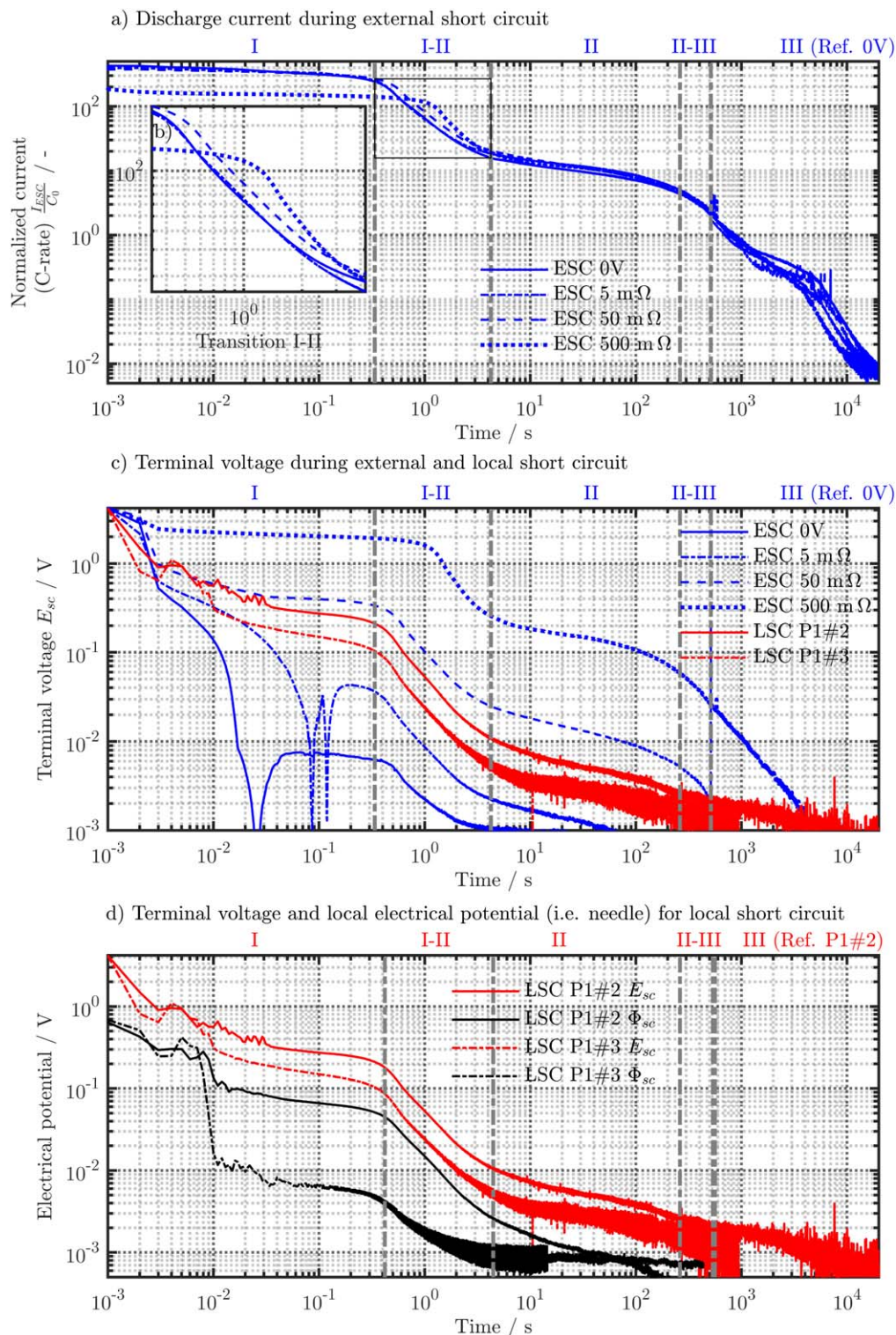
Figure 4. Normalized current (a), (b) and electrical potential (c), (d) measurement results of external (0 V as well as 5, 50, and 500 mΩ) and local (1 mm needle for P1#2 and #3) short-circuit tests applied to single-layered pouch-type cells (i.e. P1-LSC). Plateau and transition zones (I, I-II, II, II-III and III) are depicted referring to our previous works[31,32] for the 0 V ESC (a), (b), and (c) and the P1#2 LSC case (d). The electrical potential measured between the negative tab and the needle is depicted in subplot d) in reference to the terminal voltage between the positive and negative current collector tab.

Fig. 5c). To estimate the polarization/intensity for the P1-LSC cells, insights in the local potential distribution across the electrode would help to evaluate the measured potentials and to determine the difference of an externally (ESC) or locally (LSC) induced shorting on the local potential distribution.

To do so, a multidimensional multiphysics model[39–44] previously validated for the P1-type cells[32] is presented in the supplementary material and used to simulate an exemplary ESC and LSC case, which reveal a similar current flux either through the tabs or the internally shorted area in the simulation model. As the same current

Table IV. Plateau and Transition Zones of P1-type ESC and P1-LSC Tests.

Stage Cell	ESC	I	I-II	II	II-III	III
				t_{end}/s		
P1#5	0 V	0.34	4.24	262	514	end of test
P1#10	5 mΩ	0.37	4.42		537	
P1#6	50 mΩ	0.45	4.85		560	
P1#7	500 mΩ	1.03	5.47		580	
	P1—LSC					
P1#2	1 mm	0.42	4.46	between 5 and		end of test
P1#3		0.40	4.44	50 mΩ of ESC test		

flux is simulated, similar shorting resistances are expected and most likely both scenarios occur at the same short-circuit condition and shorting intensity. The resulting difference of electrical potential distribution across the electrode results in different terminal voltages, which overall occur under similar short-circuit conditions. Using the terminal voltage difference from the P1-LSC to the P1-type ESC simulation, a correction factor for the terminal voltage is derived, which accounts for the local polarization effect in the P1-LSC case and enables for its correlation to the P1-type ESC test in terms of current flux and shorting resistance.

The ESC shorting scenario simulates an external shorting of 243.9 mΩ which corresponds approximately to the P1-type cells' impedance range (see Table III) and the LSC scenario corresponds to a nail penetration similarly to the P1-LSC tests using the 1 mm needle. The resulting potential fields and transient voltage drops are shown in the supplementary material. Using the resulting correlation factor of 0.062 from the simulation results at 100 ms, the measured terminal voltage of the P1-LSC tests is corrected and the offsets to the 5 and 50 mΩ ESC tests (see Fig. 5b) are used for interpolation of the estimated shorting resistance ($R_{LSC,est}$) as shown in Table V. The 5 and 50 mΩ case were used, as the corrected P1-LSC terminal voltages from zone I to III lie in between theses cases similar as seen for the uncorrected signals in Fig. 5. The estimated shorting resistance and the corrected terminal voltage can now be used to calculate the expected current flux ($I_{LSC,est}$) at 100 ms as shown in Table V and lie in between the 5 and 50 mΩ ESC case.

A more profound analysis and discussion of the modelling and simulation part will be addressed in future as it would exceed the content of this work, but is used here to emphasize the local polarization differences, which makes a correction of the overall measured signals such as the terminal voltage necessary in order to gain a physically meaningful correlation between ESC and LSC scenarios.

To summarize, the P1-LSC test results revealed a rather hard short (see Table V and Fig. 4c) and show a very similar electrical behavior compared to the ESC tests, especially after the onset of electrochemical rate limitations (i.e. zone I-II to III). Considering the aforementioned correction for local electrode polarization, most likely an ESC test with an appropriately chosen external short-circuit resistance (see Table V) could emulate a LSC test.

Calorimetric correlation of ESC and LSC tests.—Beneficially, the actual measurement signal (i.e. temperature) for calculating the heat rate is not directly affected of the local polarization effects due to the expected thermal uniformity in the copper bars as shown in our previous works.[31,32] Hence, the P1-type ESC and P1-LSC shorting scenarios can be analyzed regarding the plateau and transition zones of the heat rate, which appears similarly to the current flux, terminal voltage, and local electrical potential (see Figs. 4a–4c) only with a certain delay in time[31] due to the inertia of heat transport phenomena and the calorimetric test bench. Figure 5 shows the calorimetric results of the P1-type ESC and P1-LSC tests after 1 s. The total heat ranges from 450 to 353 J depending on the highest to lowest capacitive cell (i.e. P1#7 and P1#2, see Fig. 5a). As the cell's capacity defines the total amount of heat,[31] the heat rate

(see Fig. 5b) is related to the cell's capacity in order to enable for a better correlation between the cells. The capacity related heat rate vs SoC of the ESC tests is shown in Fig. 5c, which helps to estimate the onset of overdischarge as shown at 100% SoC. Figure 5d magnifies the spread of heat rate where the highest external resistance shows the lowest intensity as expected. The maximum, capacity related heat rates in zone I-II can be observed for the 50 mΩ condition and the 0 V as well as the 5 mΩ case appear slightly below due to the aforementioned deviances in the cells' capacity and initial impedance (see Table III). Most interestingly, the ESC and LSC condition result in similar characteristics as shown in Fig. 5e, which allows for a correlation in the zones I-II to III exemplarily shown for the 0 V case (see also Fig. 4a). Looking into Fig. 5f, the P1-LSC results lie initially in between the 5 and 500 mΩ ESC cases and the current flux may be in between as well. The initial current flux is most likely defined by the shorting resistance (i.e. either external or at the penetration site) and the cell's impedance. For the P1-LSC, cell P1#2 indicates a lower shorting resistance due to a lower offset between the potential at the tabs and the penetration site (i.e. E_{sc} vs Φ_{sc}) and an overall slower terminal voltage decay compared to cell P1#3. As their impedances are approximately the same (see Table III), the expected higher shorting current for P1#3 results in the observed higher heat rates. Regarding stage II in Fig. 5e, the P1-LSC cases reveal lower heat rates compared to all ESC cases, which indicates higher mass transport limitations and/or variation of the short-circuit resistance. The local polarization effects (i.e. E_{sc} vs Φ_{sc}) coming with very high local currents around the penetration site or the variation[23] of the contact condition may cause the observed earlier onset of mass transport limitations, accompanied with a stronger current drop, and, consequently lower heat rates for the P1-LSC cases. Again, cell P1#2 shows a lower plateau than cell P1#3 due to the aforementioned difference in shorting resistance and resulting current flux.

Comparing all P1-LSC tests, the initial impedances (see Table III) vary in the range from 298.7 (P1#9) to ≈360 mΩ (P1#2 and #3) as well as the cell's capacities (28.1, 17.1, and 19.1 mAh). Regarding the resulting heat generation rate profiles, the higher the impedance and the lower the capacity, the lower the initial current in zone I-II, and the higher the subsequent mass transport limitations accompanied with lower heat rates in zone II. Note, that also the altering contact condition during the short-circuit may most likely affect the heat generation rate profile. Unfortunately, none of the tested P1-LSC cells revealed a similar, initial impedance as the P1-type ESC cells. Most likely, the applied pressure condition between

Table V. Estimated Shorting Resistance and Current Flux for P1-LSC Tests at 100 ms.

$t = 100$ ms	Resistance $R_{LSC,est}$/mΩ	Current $I_{LSC,est}$/A
P1#2	38.7	7.5
P1#3	24.5	6.4
P1#9	40.9	7.6

est = estimated.
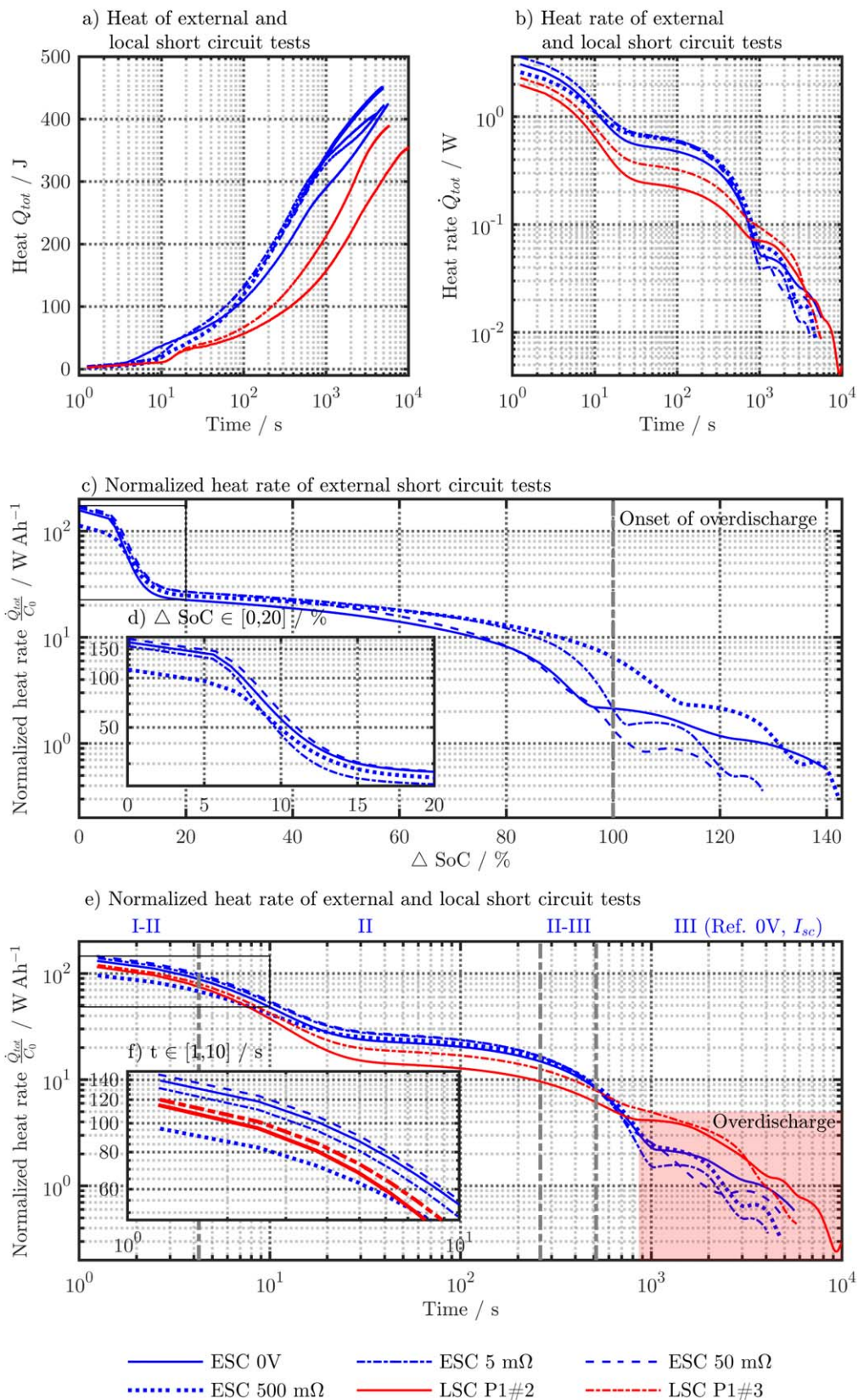
Figure 5. Calorimetric measurements of ESC and LSC applied to single-layered pouch-type cells (i.e. P1-LSC). Subplot (a) and (b) show the total amount of heat (Q_{tot}) and the heat rate ($\dot{Q}_{tot}$). Subplot (c) shows the heat rate related to the cell's capacity vs the SoC with a magnified area (d) between 0 and 20% for all ESC tests. Subplot (e) shows the related heat rates vs time with a magnified area (f) between 1 and 10 s. For comparison, the zones I-II to III are depicted as shown in Fig. 4a for the 0 V case, referring to the measured current flux (I_{sc}).

Table VI. Nomenclature.

Latin symbols

C_p	J K^{-1}	Heat capacity
C_0	Ah	Initial capacity at 0.5 C CC discharge
C_{sc}	Ah	Discharged capacity after the ESC test
d	m	Diameter of nail (i.e. stainless steel needle)
E_{eq}	V	Equilibrium potential vs Li/Li$^+$
E_{sc}	V	Terminal voltage
$E_{sc,end}$	V	Terminal voltage after the short-circuit test
F	96 485 As mol^{-1}	Faraday's constant
I_{sc}	A	Current flux during short-circuit scenario
$I_{LSC,est}$	A	Estimated current flux for LSC test
I_{max}	A	Maximum current flux for ESC test
m	kg	Mass of cell
R	8.314 J mol^{-1} K^{-1}	Gas constant
R_{ext}	Ω	External resistance for ESC test
$R_{i,0}$	Ω	Initial impedance from EIS measurement
$R_{i,sc}$	Ω	Final impedance from EIS measurement after the short-circuit test
$R_{LSC,est}$	Ω	Estimated shorting resistance of LSC test
$\dot{Q}_{tot}^*$	W	Uncorrected heat generation rate
$\dot{Q}_{tot}$	W	Calorimetric-corrected heat generation rate
Q_{tot}^*	W	Uncorrected total amount of heat
Q_{tot}	W	Calorimetric-corrected total amount of heat
t	s	Time
T	K	Temperature
Greek symbols		
Φ_{sc}	V	Electrical potential between the penetration site vs the cell's negative tab

the copper bars during the short-circuit experiments influenced the impedance of the cells, which will be investigated in the future. Regarding zones II-III (see Fig. 6d) and III, similar heat rate decays for the ESCs and the P1#9 LSC case appear due to the lower potential, heat rate and expected current flux plateau during zone II compared to the cells P1#2 and #3. Interpreting the P1-LSC tests using the calorimetric results may reveal a slightly more inaccurate correlation to the P1-type ESC tests (i.e. between 5 and 500 mΩ), but helps to better understand the correlation of the cell's initial impedance, initial capacity and the shorting resistance at the penetration site during the short-circuit scenario.

LSC applied to double-layered pouch-type cells.—To investigate LSCs occurring simultaneously in multiple electrode layers, nail penetration is applied in the P2-LSC tests to trigger short-circuits in both electrode stacks. In comparison, only a single electrode stack is penetrated with the nail in the P3/P4-coupled LSC/ESC tests and the second one undergoes an ESC via the current collector path.

Figure 7 shows the resulting terminal voltages of the P2-LSC and P3/P4-LSC/ESC in reference to the P1-type ESC and P1-LSC cases. After the attenuation of mechanical oscillations of the short-circuit device, all LSC tests (P2, P3, and P4) lie in between the 50 and 500 mΩ ESC case (i.e. from zone I to II-III ref. to the 50 mΩ case) until the onset of zone III. At the transition I-II, the P2-LSC shows faster voltage decrease compared to the P3/P4-LSC/ESC tests, which more or less show no significant difference in their electrical behavior. From zone II until III, the P3/P4-LSC/ESC test approach the 500 mΩ ESC case, which indicates a higher ohmic resistance behavior caused by lower mass transport limitations during zone II. The P2-LSC shows increased mass transport limitations during zone II and a faster voltage decay, and remains in between the aforementioned ESC cases.

Ideally, similar contact conditions in both penetration sites of the P2-LSC test should be achieved and the terminal voltage should assimilate the P1-LSC test. At the very beginning ($\approx$2 ms), the lower initial impedance and the higher capacity of P2#1 (see Table III) compared to the P1#2 cell leads to a lower onset of the terminal voltage during zone I and a higher initial current peak is expected. During zone I, the contact condition in both electrode layers most likely forms/alters and results in a higher ohmic resistance behavior, which leads to the subsequent offset from zone I-II to III. As a result, non-ideal penetration may lead to a higher ohmic contact condition in one or both electrode stacks, when two stacks are penetrated at once.

The P3- and P4-type cells' impedances differ (see Table III), which leads to the appearing marginal lower voltage plateau of P4#1 compared to P3#2 in zone I, but overall no significant difference in the electrical behavior appears. The higher ohmic resistance behavior during the transition zone I-II is probably correlated to the simultaneous ESC in the second electrode stack. As no difference between the P3 and P4 case were observed, penetrating first the anode or the cathode has negligible influence on the resulting shorting behavior.

The total amount of heat is shown in Fig. 8a and totals of 874, 821, and 799 J for the P2-LSC, the P3, and P4-LSC/ESC test appear. Relating the heat rates shown in Fig. 8b to the cell capacity, Fig. 8c allows to evaluate the shorting scenarios as discussed for the P1-type cells. Beside the contact condition at the penetration site, higher capacity and lower impedances (see Table IIId) most likely lead to higher initial currents in stage I-II compared to the P1-type cells. Similar mass transport limitations appear for the P2- and P4-type cell shown in Fig. 8e, which assimilate the 50 mΩ ESC case until zone II-III. The P3-type LSC test shows slightly increased mass transport limitations resulting in a marginal lower heat rate plateau in zone II, similar to the P1-type LSC test. Analyzing the electrical potential at the penetration site for the P3-type cell, a slightly higher offset to the terminal voltage appeared compared to the P2- and P4-type cells, which indicates an increased local polarization across the electrodes
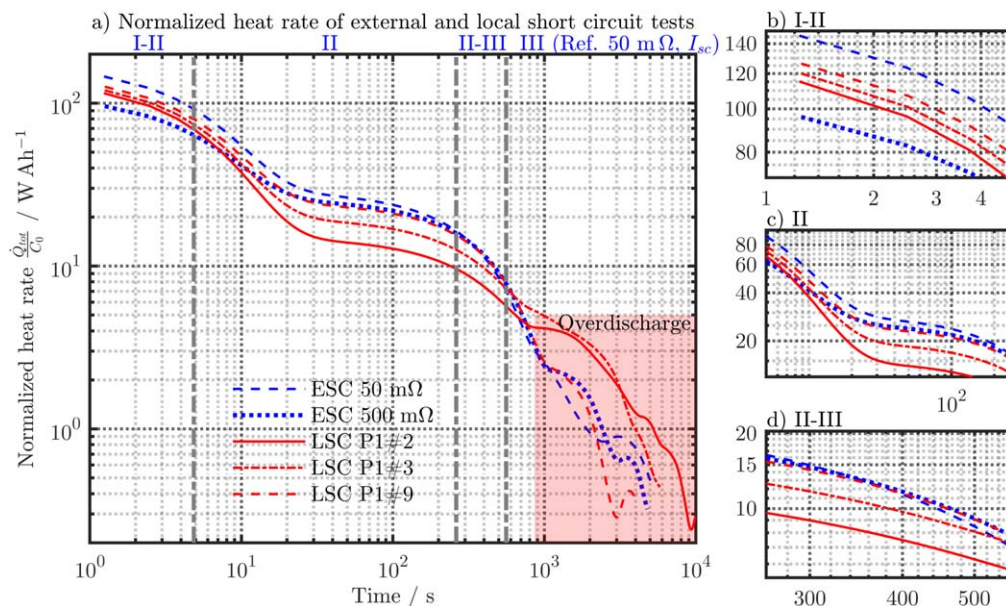
Figure 6. Capacity related heat generation rate of the P1-type ESC (50 and 500 mΩ) and P1-LSC tests. Subplot (a) shows the related heat rates of ESC and LSC tests over time with magnified areas (b)–(d) referring to the zones I-II, II, and II-III of the 50 mΩ case (I_{sc}).
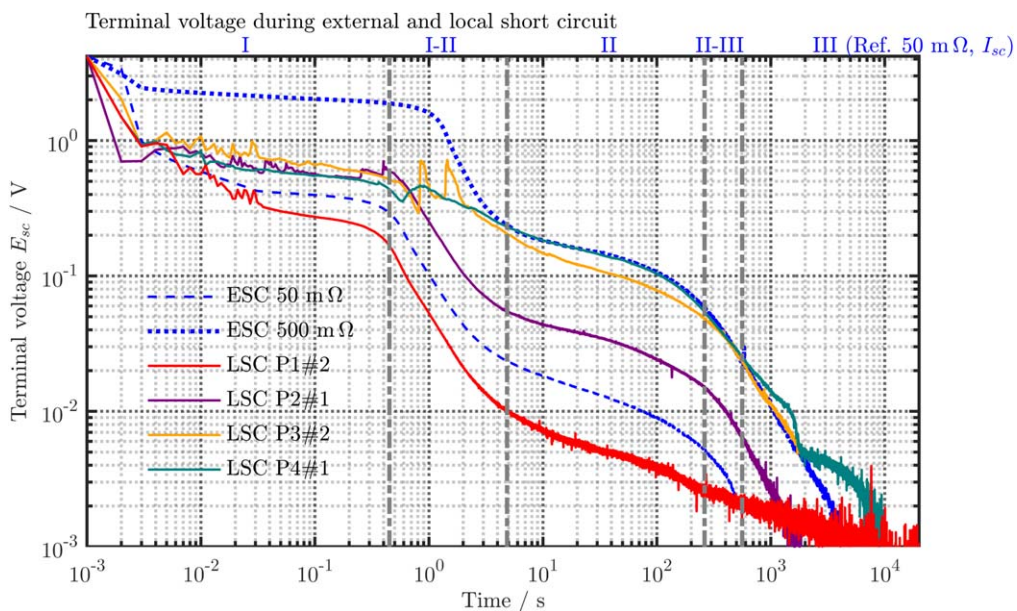

Figure 7. Measurement results showing the terminal voltage of ESC (50 and 500 mΩ, only configuration P1) and LSC (1 mm needle) tests applied to single-(P1#2) as well as double-layered (P2# 1, P3#2, and P4#1) pouch-type cells. Plateau and transition zones (I, I-II, II, II-III and III) are depicted referring to the 50 mΩ ESC case.

and therefore increases the limitation behavior as discussed before. This corresponds to the slightly lower terminal voltage plateau of the P3-type cell shown in zone II (see Fig. 7). As the current flux during zone II is most likely higher for all double-layered cells compared to the P1-LSC cells, faster discharge/voltage decay appears in zone II-III (see Fig. 8f) similar to the P1-type 50 mΩ ESC case. From zone I-II to II-III, the P2-LSC cell shows higher heat rates than the P3/P4-type cells which corresponds to the terminal voltage profiles in Fig. 7, and ends in zone III with the fastest discharge/limitation of the P2-LSC cell. To conclude, the results of the P2-LSC test revealed an unexpected offset to the P1-LSC test, which is most likely caused by non-similar contact condition in one or both penetrated electrode stacks. Penetrating both (P2-LSC) or only a

single electrode stack (P3/P4-coupled LSC/ESC) in a double-layered test cell, revealed significant differences for the terminal voltage profile after the transition zone I-II, which corresponds to the observed capacity related heat rate profile. The actual local shorting conditions (i.e. either LSC applied to all electrode stacks or a single LSC in one electrode stack leading to a subsequent ESC in the remaining one) must therefore be considered, when the results of a nail/needle penetration test are interpreted in terms of emulating ISC scenarios in LIBs.

LSC applied to double-layered pouch-type cells using various needle diameter.—P2-type LSCs are applied with a needle of 0.5, 1, and 2 mm to analyze the correlation of penetration size, the resulting
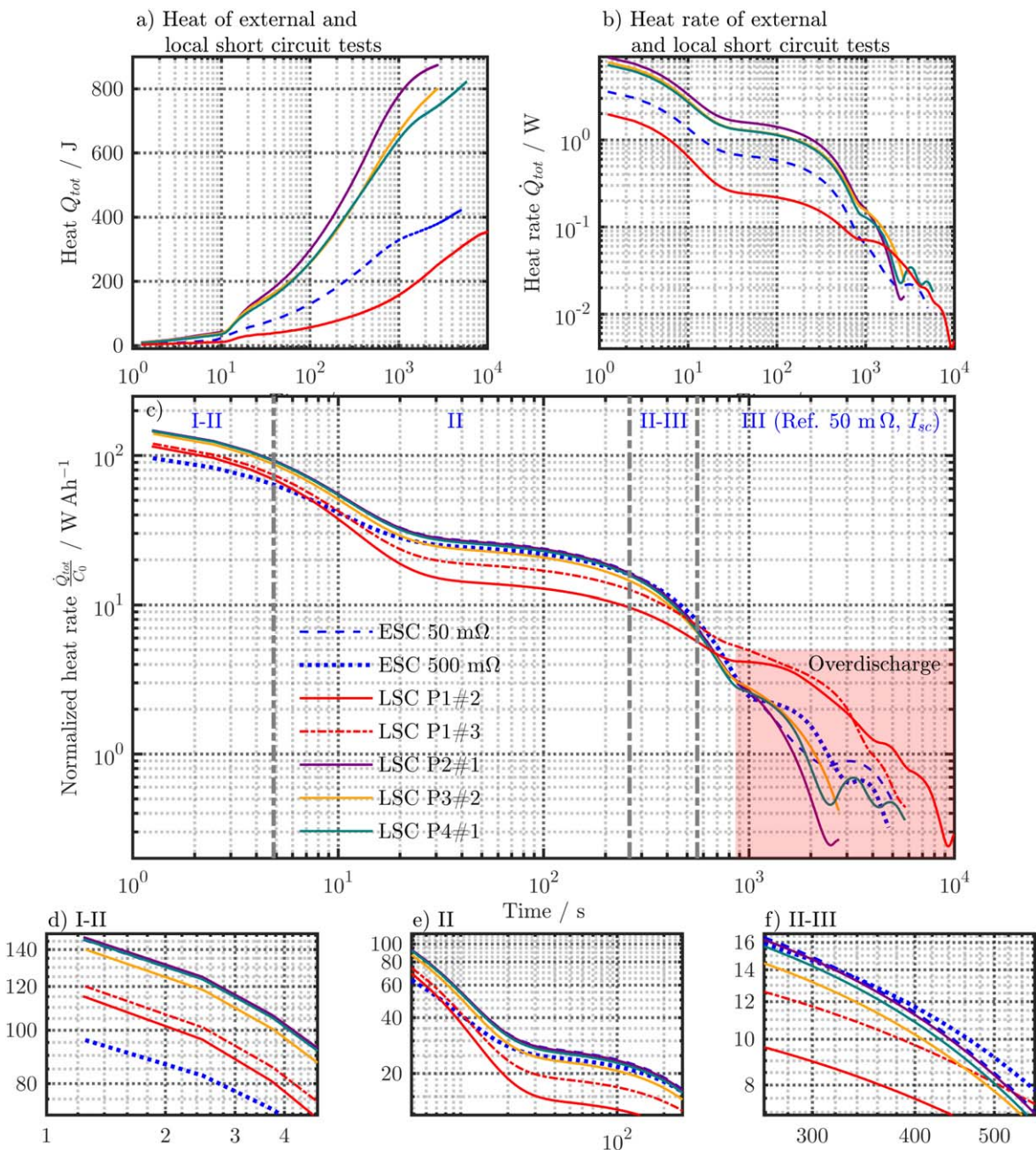
Figure 8. Calorimetric measurements of the P2-LSC and P3/P4-coupled LSC/ESC tests in comparison to the P1-type ESC and P1-LSC tests. Subplot a) and b) show the total amount of heat (Q_{tot}) and the heat rate ($\dot{Q}_{tot}$). Subplot c) shows the capacity related heat generation rates $\left(\frac{\dot{Q}_{tot}}{C_0}\right)$ with magnifications for zone I-II (d), II (e), and II-III (f). The zones I-II to III are depicted as shown in Fig. 4 for the 50 mΩ case, referring to the measured current (I_{sc}).

contact condition, and the appearing short-circuit intensity. Figure 9 shows the capacity related heat rates in comparison to the P1-type ESC and P1-LSC cases.

Regarding zone I-II in Fig. 9b, the 2 mm case reveals the highest (>160 W Ah^{-1}) heat rate, the 0.5 mm case the lowest ($\approx$120 W Ah^{-1}) heat rate but higher than the 500 mΩ ESC as well as the P1-LSC cases, and the 1 mm case lies in between these two cases, assimilating the 50 mΩ case as discussed before. Considering the cells' impedances and the capacities (see Table III), most likely the resulting maximum heat rates in zone I-II correlate well with the diameter of the needle as: The larger the diameter of the needle, the higher the heat rate and the underlying shorting intensity. Regarding zone II in Fig. 9c, increased mass transport limitations are seen for the 2 mm case, which shows the lowest heat rates compared to the 1 and 0.5 mm case, and the lowest mass transport limitation are seen for the 0.5 mm case. Due to the

highest capacity, the cell applied with 1 mm shows the slowest heat rate decay in zone II-III (see Fig. 9d) compared to the 0.5 and 2 mm case. As a conclusion, the intensity of the LSC test is directly affected by the shorted area in the penetration site, which correlates well with the chosen needle diameter.

Post-mortem analysis.—*Post-mortem* analysis by means of visual inspection, SEM, and EDX is applied to cells used in the ESC and the LSC tests in order to evaluate the degradation of the graphite and NMC-111 electrodes. Similar results were observed for all studied cells depicted in the supplementary material and the results of cell P1#10 (ESC at 5 mΩ) and P1#2 (LSC with 1 mm) are presented in the following.

Figure 10 shows the opened cell P1#10 revealing partly delamination of the graphite composite electrode (a) and a
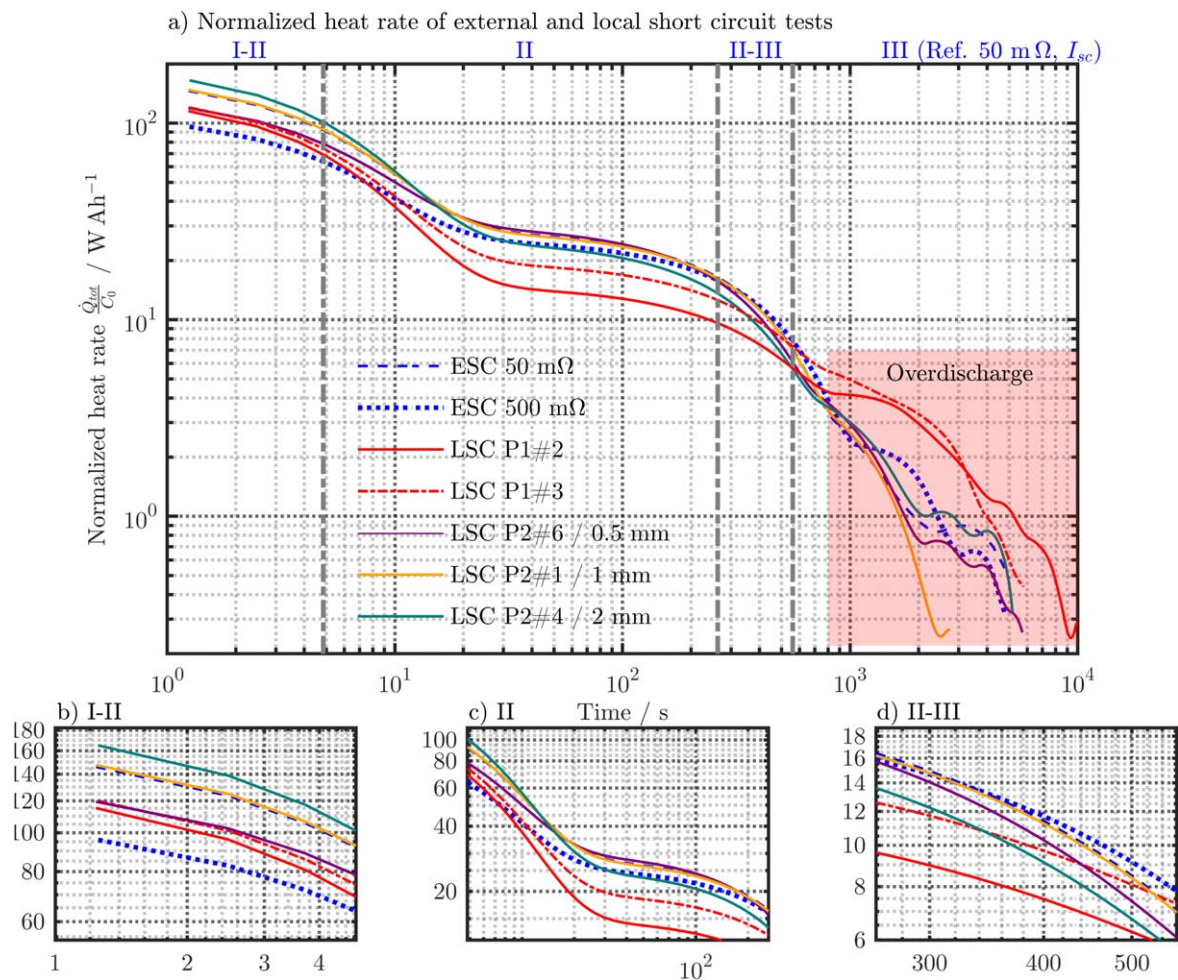
Figure 9. Capacity related heat rate of the varying needle diameter tests applied to P2-type cells. Diameters of 0.5, 1, and 2 mm tests are shown in comparison to the P1-type ESC (50 and 500 mΩ) and P1-LSC tests using a 1 mm needle applied to P1-type cells. The plateau and transition zones are shown in reference to 50 mΩ ESC case (I_{sc}).

mechanically rather intact NMC-111 cathode (b). Magnifications (see Figs. 10c and 10d) at a factor of 1000 show SEM images of the electrode surface revealing depositions on the anode and cracked or even burst NMC-111 active material particles on the cathode as discussed in our previous work.[31] Applying EDX measurements at these positions (e to h) indicates significant amounts of copper on both electrodes, which is not the case for the pristine materials (i to l) before the ESC. Low lithiation levels and high overpotentials in the anode most likely cause copper dissolution from the negative current collector during the ESC and subsequent deposition across the electrodes as impurities during disassembly, handling and preparation during the *post-mortem* analysis could be excluded. Most likely, the deposition of copper in the anode is caused by significant potential differences through the thickness of the graphite coating during the short-circuit and in the cathode by its higher potential levels. The amount of oxygen is most likely caused by handling the samples outside the argon-filled glove box and the carbon content is referred to the actual active material (f, i) and the content of binder (h, l). Regarding the P1-LSC test of cell P1#2 shown in Figs. 11 and 12, the graphite anode in Fig. 11a clearly shows delamination of its composite material and looking into the magnifications near the tab (b, x50) and near the bottom (h, x500), entire holes (≈⌀ 129.6 μm) or partly surficial dissolutions (≈⌀ 3.2 μm) appear (see 11i) where copper is completely or partly dissolved. Magnifications near the penetration site (c) reveal deep radial cracks through the thickness of the graphite composite, which indicates significant amounts of copper (d and e) compared to the pristine material (f and g).

Around the penetration site, all cells showed complete dissolution of the copper foil, which indicates the highest current densities and overpotentials and thus maximum local intensity of the shorting scenario. Similar to the ESC analysis, copper dissolution and deposition could be observed at strongly delaminated spots across the anode, where the coating came off during disassembly. Beside cracked or burst active material particles of the NMC-111 cathode shown in Fig. 12, no delamination but deep cracks were observed throughout the coating (SEM x150 and x1000, h and i) near the penetration site, which underlines a higher local intensity of the shorting scenario. The magnification in b (SEM × 40) shows the penetration site itself with clear marks of cutting and crumpling of the cathode caused by the needle penetration. A magnification (SEM x500, c) offers a cross view analysis through the coating thickness as shown in Fig. 12e (SEM × 1000, see d). Compared to the pristine material (f and g), contents of copper are significantly indicated not only on the surface of the electrode, but also throughout the entire thickness of the cathode as well as near the aluminum current collector. Overall, significantly increased indications of copper dissolution and deposition can be observed throughout the coating thickness as well as across both anode and cathode. As the LSC tests result in a deeper discharge condition compared to the ESC test (i.e. ESC stops at I_{sc} < 0.1 mA), the observed increased intensity of copper dissolution and deposition seems justified. The expected intense locality appearing in the LSC scenario was shown by complete dissolution of the copper current collector around the penetration site and increased degradation signs in the NMC-111 cathode.
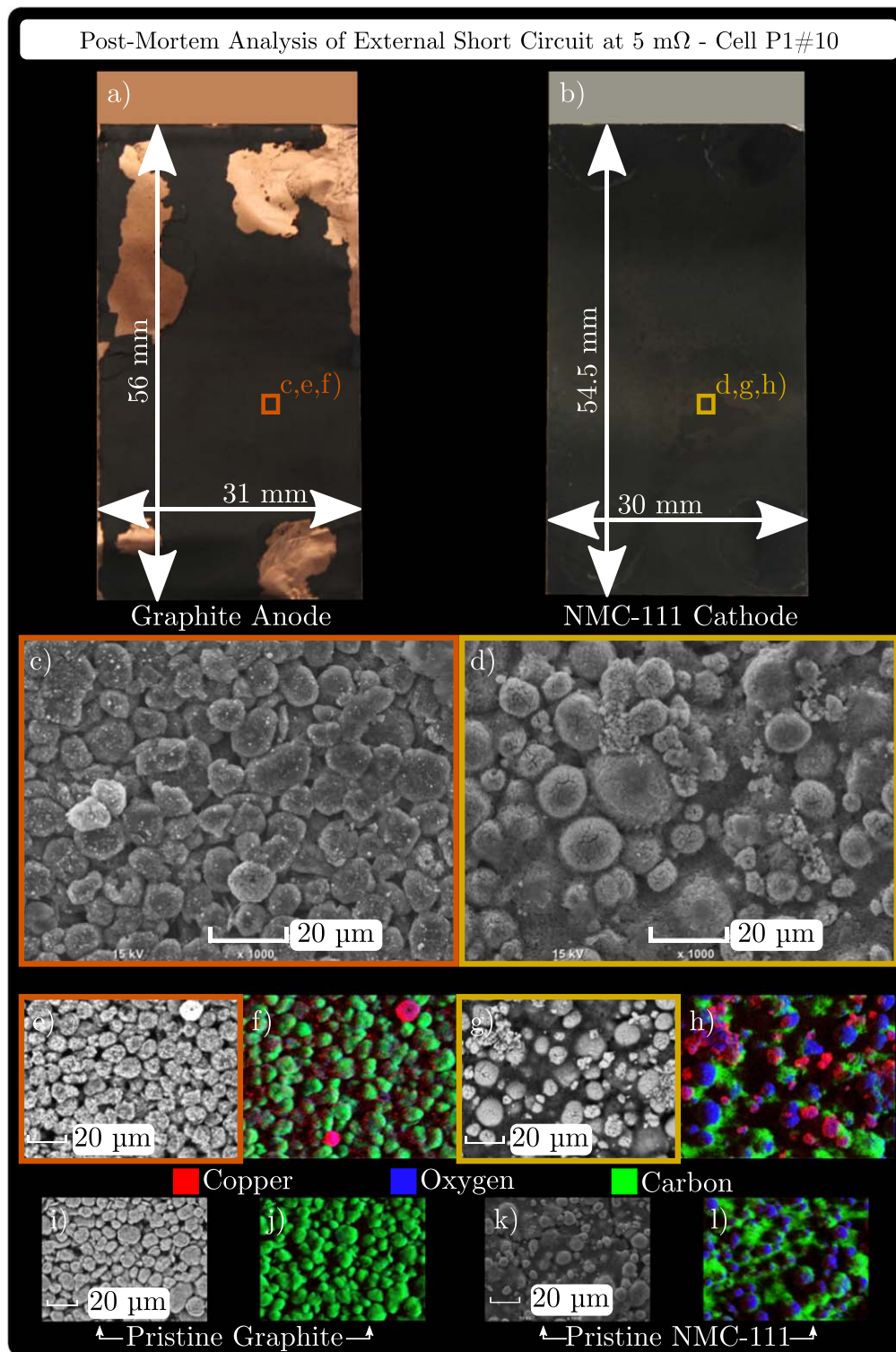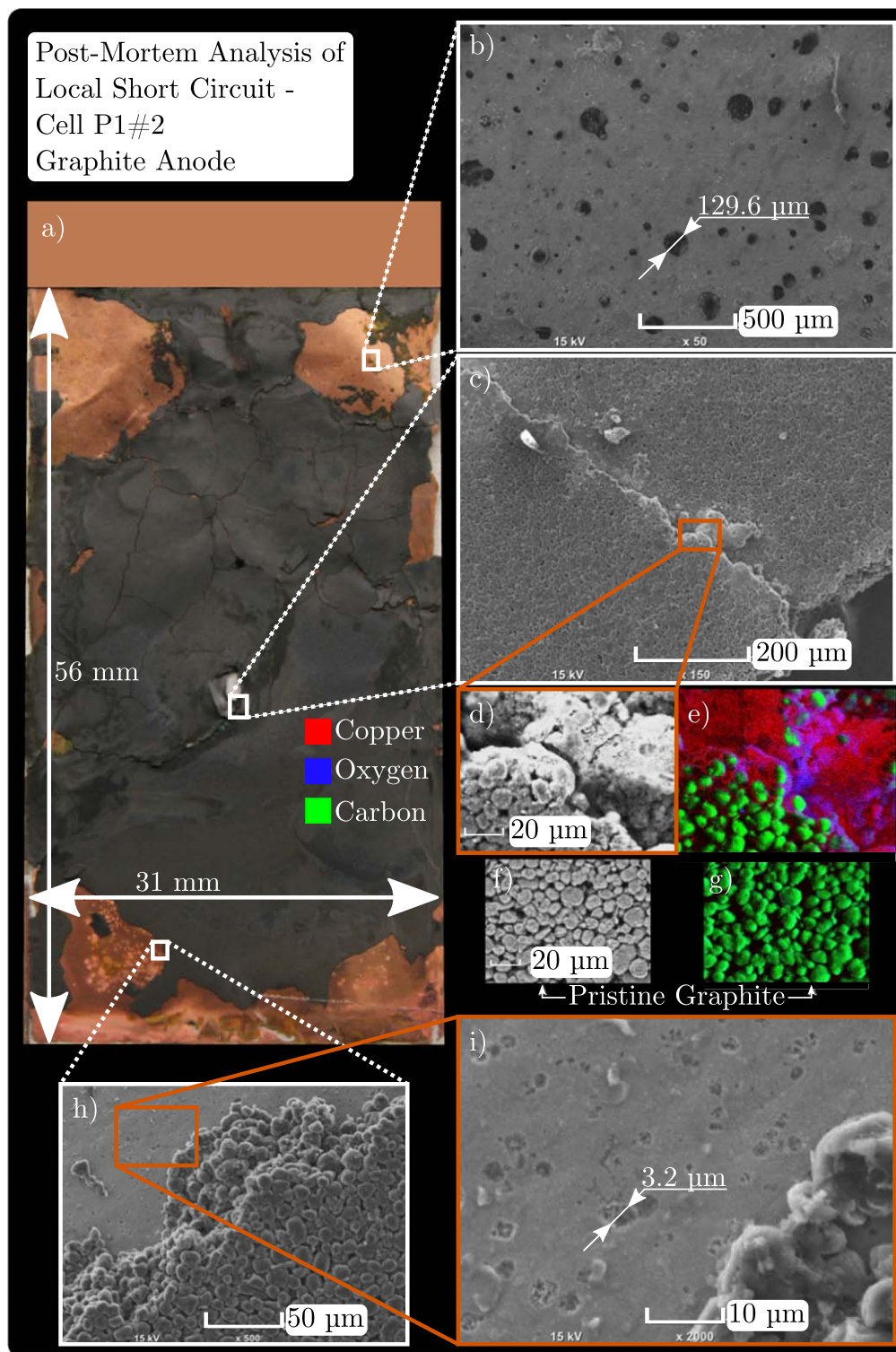
Figure 10. *Post-mortem* analysis of cell P1#10 after the applied ESC at 5 mΩ showing images of the entire anode (a) and cathode (b), magnified (SEM × 1000) spots (marked in orange and gold) on each electrode (e to h), and their EDX analysis in comparison to the pristine electrodes (i to l) showing contents of copper (red), oxygen (blue), and carbon (green).

Conclusions

The electrical and thermal short-circuit behavior of externally and locally applied short-circuits (i.e. needle/nail penetration) was investigated on single or double-layered graphite/NMC-111 pouch-type LIBs using a quasi-isothermal, calorimetric test bench. The quasi-isothermal short-circuit conditions enable for analyzing the electrical and thermal short-circuit behavior without triggering a high local heat generation rate, which may lead to thermal, self-accelerating processes such as a thermal runaway scenario. By applying our technique, we can mitigate the influence of such local, thermal effects and analyze the pure electrical short-circuit behavior in the very beginning (i.e. zone I) until various current rate limitation effects (i.e. zones I-II to III) appear,

Figure 11. *Post-mortem* analysis of cell P1#2 after the P1-LSC test showing the entire graphite anode (a) and magnified sites near the tab (SEM x50, b), the penetration site (SEM × 150, c), and at the bottom (SEM x500, h) depicting holes in the copper current collector, cracks through the electrode or initially dissolved copper sites (SEM x2000, i), respectively. The crack shown in c) is magnified (SEM x2000, f) for EDX analysis (e) revealing significant contents of copper compared to the pristine material shown in f) and g) before the P1-LSC test.

which are caused by either the anode or the cathode within the tested cells. Comparing the P1-type ESC and LSC results in the very beginning of the short-circuit (i.e. zone I), differences in the electrical behavior were seen but as soon as electrochemical rate limitation effects within both the anode and the cathode initiate (i.e. from zone I-II to III), the electrical behavior shows similar damping characteristics. As a result, the locality of the short-circuit defines the electrical behavior in the very beginning (i.e. <1 s, zone I), but the subsequent rate limitation effects proceed similarly for the ESC and the LSC test. The observed hard short-circuit conditions caused by the needle penetration can thus be emulated by an ESC test with an appropriately chosen external short-circuit resistance for the very beginning (i.e. zone I), which also accounts for the discussed terminal voltage variance calculated from the presented simulation results. The measured local
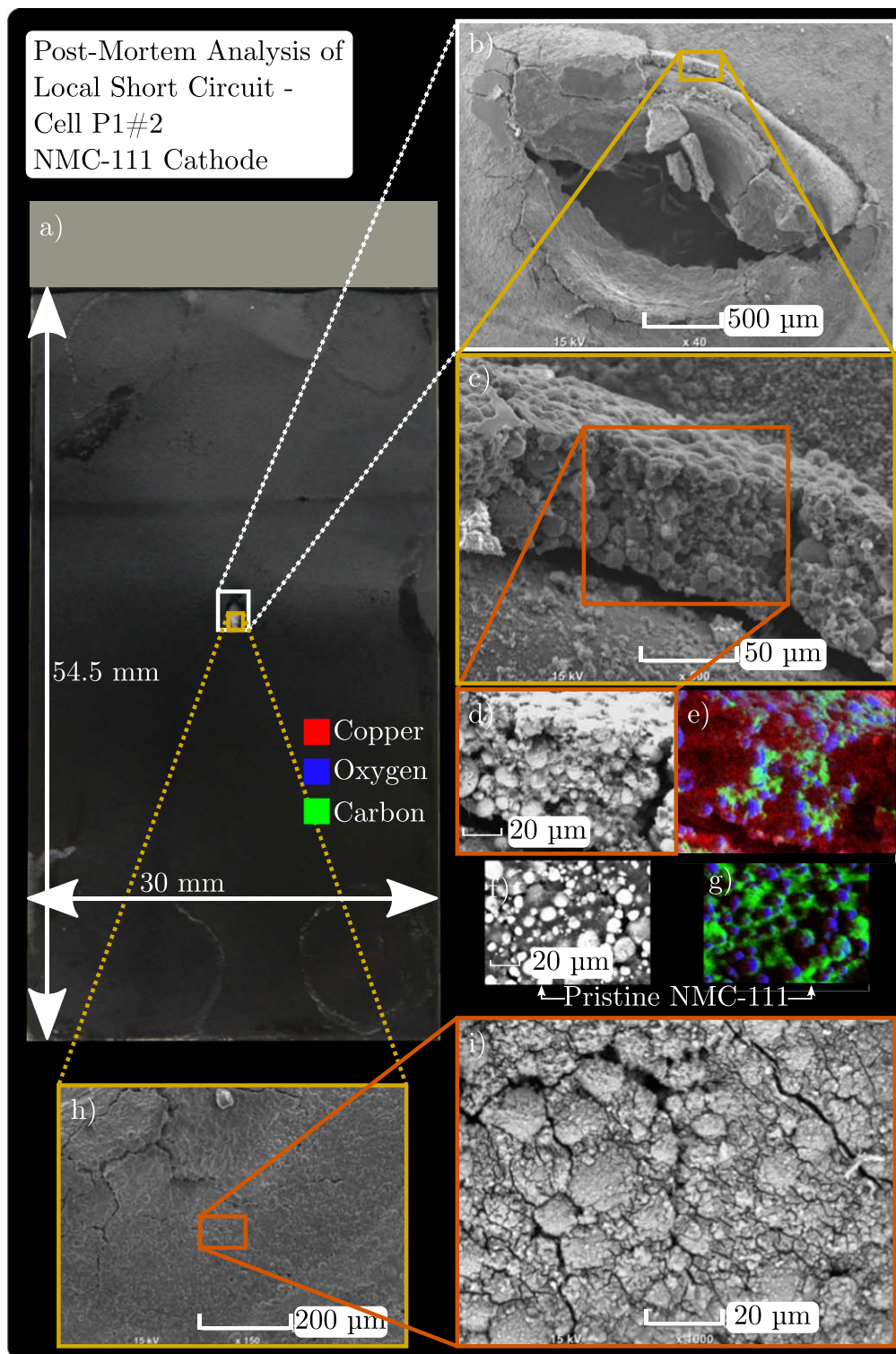
Figure 12. *Post-mortem* analysis of cell P1#2 after the P1-LSC test showing the entire NMC-111 cathode (a) and magnified sites near the penetration area (SEM x150/x1000 in h/i and SEM x40 in c). The penetration site in b) reveals cut (bottom) and crumpled (top) areas (SEM x40) and EDX applied over the coating thickness (SEM x500/x1000, c/d) indicates significant copper content (e) compared to the pristine cathode (SEM x1000, f and g) before the P1-LSC test.

potential at the penetration site via the electrically connected needle vs the cell's negative tab shows the same characteristics as the measured terminal voltage, only with a significant potential offset caused by electrode polarization, current flux over the needle, and the altering short-circuit contact condition. Most likely, the differently appearing potential offsets in the P1-LSC tests may be correlated to a higher or lower current flux around the penetration site and may indicate higher

or lower polarization effects in the cell and thus can be used to evaluate the local short-circuit intensity at the penetration site. Overall, a cells' initial impedance, initial capacity and the electrical contact condition at the penetration site mainly determine the electrical and thermal LSC behavior resulting in a higher or lower current rate limitation behavior. The ESC test offers higher reproducibility, practicability of the actual measurement, and can emulate a LSC scenario in terminal voltage and

heat rate profile. Based on these results, the presented ESC test method is recommended not only to emulate external short-circuits, but also local/internal short-circuit scenarios in LIBs.

Applying needle penetration to both electrode stacks in double-layered cells (i.e. P2-LSC), only marginal differences were observed for the electrical behavior in the very beginning (i.e. <1 s, zone I) compared to a short-circuit applied to a single electrode stack, which triggers an external short-circuit on the second one (i.e. P3/P4—coupled LSC/ESC). However, a significant difference in the electrochemical rate limitation behavior was observed subsequently (i.e. >1 s, zone I-II to III), which indicates reduced rate limitation effects for a coupled LSC/ESC case. Increasing the shorting area investigated via various needle diameters (i.e. 0.5, 1, and 2 mm) leads to higher heat generation rates, which correlates well to a more intensive short-circuit or so called harder short. Similar to the single-layered cells, capacity, impedance, and contact condition determine the short-circuit intensity where the latter shows severe dependency on the used needle diameter as well as the number of penetrated electrode stacks as seen from the results of the double-layered cells.

Overdischarge of the cells appeared in all tests as indicated via initial DVA and finally correlated to copper dissolution/deposition across both active areas of the electrodes analyzing the results of SEM and EDX measurements. Regarding the LSC tests, increased local degradation around the penetration site appeared and a deeper discharge resulting in more intense copper detection indicate the highly local polarization and longer exposure to high current conditions compared to the ESC tests.

Future work will focus on statistical relevance of the presented LSC tests regarding the variance of contact conditions within the penetration site and multidimensional multiphysics simulation studies of LSC and ESC scenarios in order to investigate the difference in local polarization effects throughout and across the electrodes.

Acknowledgments

Appendix

ORCID

J. Sturm https://orcid.org/0000-0001-8876-9989
A. Rheinfeld https://orcid.org/0000-0003-0995-7266

References

1. FAA Office of Security and Hazardous Materials Safety, *Lithium Batteries & Lithium Battery-Powered Devices*, FAA Office of Security and Hazardous Materials Safety - United States Department of Transportation, Federal Aviation Administration (2019), https://faa.gov/hazmat/resources/lithium_batteries/media/Battery_incident_chart.pdf.
2. M. J. Kolly, J. Panagiotou, and B. A. Czech, *The Investigation of a Lithium-Ion Battery Fire Onboard a Boeing 787 by the US National Transportation Safety Board*, National Transportation Safety Board (2013), https://ntsb.gov/investigations/pages/boeing_787.aspx.
3. M. P. Huerta, *Safety Recommendation A-14-032 through -036*, National Transportation Safety Board (2014), https://ntsb.gov/investigations/pages/boeing_787.aspx.
4. D. A. P. Hersman, *Investigative Update of Battery Fire Japan Airlines B-787*, National Transportation Safety Board (2013), https://ntsb.gov/investigations/pages/boeing_787.aspx.
5. S. Tobishima, *Encyclopedia of Electrochemical Power Sources*, ed. J. Garche and C. K. Dyer (Academic Press and Imprint of Elsevier, Amsterdam and Boston) (2009), https://elsevier.com/books/encyclopedia-of-electrochemical-power-sources/garche/978-0-444-52093-7.
6. K. White, *Samsung Recall Support Note7 Investigation*, Exponent—Engineering and Scientific Consulting (2017), https://news.samsung.com/global/wp-content/themes/btr_newsroom/download.php?id=E0RaV5Kg8MHmLtmcg%2BD%2BJXcIe2h9FIPFzKNa3EsW0Ao%3D.
7. Samsung Electronics, *Galaxy Note7 What we discovered*, Samsung Electronics (2017), https://news.samsung.com/us/Samsung-Electronics-Announces-Cause-of-Galaxy-Note7-Incidents-in-Press-Conference.
8. S. Abada, G. Marlair, A. Lecocq, M. Petit, V. Sauvant-Moynot, and F. Huet, *Journal of Power Sources*, **306**, 178 (2016).
9. G. E. Blomgren, *J. Electrochem. Soc.*, **164**, A5019 (2017).
10. D. Andre, S.-J. Kim, P. Lamp, S. F. Lux, F. Maglia, O. Paschos, and B. Stiaszny, *Journal of Materials Chemistry A*, **3**, 6709 (2015).
11. J. B. Habedank, L. Kraft, A. Rheinfeld, C. Krezdorn, A. Jossen, and M. F. Zaeh, *J. Electrochem. Soc.*, **165**, A1563 (2018).
12. V. Ruiz, A. Pfrang, A. Kriston, N. Omar, P. van den Bossche, and L. Boon-Brett, *Renew. Sustain. Energy Rev.*, **81**, 1427 (2018).
13. A. Rheinfeld, *Performance and Safety of Lithium-Ion Electrodes and Cells: Modeling, Simulation, and Validation at Elevated Temperatures and Currents*, Technical University of Munich, Department of Electrical and Computer Engineering, Institute for Electrical Energy Storage Technology (2019), Ph.D.-Thesis http://nbn-resolving.de/urn/resolver.pl?urn:nbn:de:bvb:91-diss-20190920-1506354-1-9.
14. C. J. Orendorff, "The Role of Separators in Lithium-Ion Cell Safety." *The Electrochemical Society Interface*, **21**, 2 (2012) .
15. J. A. Jeevarajan, J. Collins, and J. S. Cook, *Safety Evaluation of two commercial lithium-ion batteries for space applications*, NASA-Johnson Space Center (2004), https://ntrs.nasa.gov/archive/nasa/casi.ntrs.nasa.gov/20050217484.pdf.
16. R. Bisschop, O. Willstrand, F. Amon, and M. Rosengren, *Fire Safety of Lithium-Ion Batteries in Road Vehicles 2019:50*, RISE Research Institutes of Sweden AB (2019), http://diva-portal.org/smash/get/diva2:1317419/FULLTEXT02.
17. A. Abaza, S. Ferrari, H. K. Wong, C. Lyness, A. Moore, J. Weaving, M. Blanco-Martin, R. Dashwood, and R. Bhagat, *Journal of Energy Storage*, **16**, 211 (2018).
18. C. T. Love, O. A. Baturina, and K. E. Swider-Lyons, *ECS Electrochem. Lett.*, **4**, A24 (2014).
19. Y. Zhu et al., *Nat. Commun.*, **10**, 2067 (2019).
20. B. Barnett, D. Ofer, S. Sriramulu, and R. Stringfellow, *Encyclopedia of Sustainability Science and Technology*, ed. R. A. Meyers (Springer, New York and London) p.6097 (2012).
21. T. Yokoshima, D. Mukoyama, F. Maeda, T. Osaka, K. Takazawa, and S. Egusa, *J. Electrochem. Soc.*, **166**, A1243 (2019).
22. C. J. Orendorff, E. P. Roth, and G. Nagasubramanian, *Journal of Power Sources*, **196**, 6554 (2011).
23. S. Santhanagopalan, P. Ramadass, and J. Zhang, *Journal of Power Sources*, **194**, 550 (2009).
24. C.-S. Kim, J.-S. Yoo, K.-M. Jeong, K. Kim, and C.-W. Yi, *Journal of Power Sources*, **289**, 41 (2015).
25. D. P. Finegan, B. Tjaden, T. M. M. Heenan, R. Jervis, M. Di Michiel, A. Rack, G. Hinds, D. J. L. Brett, and P. R. Shearing, *J. Electrochem. Soc.*, **164**, A3285 (2017).
26. T. D. Hatchard, S. Trussler, and J. R. Dahn, *Journal of Power Sources*, **247**, 821 (2014).
27. P. Porampojana, *Experimental investigation of internal short circuits in lithium-ion batteries*, The Pennsylvania State University (2015), Ph.D.-Thesis https://etda.libraries.psu.edu/files/final_submissions/11020.
28. T. R. Tanim, M. Garg, and C. d. Rahn, *An Intelligent Nail Design for Lithium Ion Battery Penetration Test. ASME 2016 X International Conference on Energy Sustainability collocated with the ASME 2016 Power Conference and the ASME 2016 XIV International Conference on Fuel Cell Science, Engineering and Technology*, New York, N.Y. p. V002T01A001 (2016).
29. T. Yokoshima, D. Mukoyama, F. Maeda, T. Osaka, K. Takazawa, S. Egusa, S. Naoi, S. Ishikura, and K. Yamamoto, *Journal of Power Sources*, **393**, 67 (2018).
30. T. Volck et al., *Batteries*, **2**, 8 (2016).
31. A. Rheinfeld, A. Noel, J. Wilhelm, A. Kriston, A. Pfrang, and A. Jossen, *J. Electrochem. Soc.*, **165**, A3427 (2018).
32. A. Rheinfeld, J. Sturm, A. Noel, J. Wilhelm, A. Kriston, A. Pfrang, and A. Jossen, *J. Electrochem. Soc.*, **166**, A151 (2019).
33. A. Kriston, A. Pfrang, H. Döring, B. Fritsch, V. Ruiz, I. Adanouj, T. Kosmidou, J. Ungeheuer, and L. Boon-Brett, *Journal of Power Sources*, **361**, 170 (2017).
34. A. Rheinfeld, S. Kosch, S. V. Erhard, P. J. Osswald, B. Rieger, and A. Jossen, *J. Electrochem. Soc.*, **163**, A3046 (2016).
35. Otto Ganter GmbH & Co. KG, (2018), Indexing plunger https://ganternorm.com/de/produkte/3.1-Rasten-Arretieren-Sperren-mit-Bolzen-und-Kugeln/Rastbolzen-Arretierbolzen/GN-817.9-Rastbolzen-demontierbar-mit-und-ohne-Rastsperre.
36. H. Maleki, *J. Electrochem. Soc.*, **146**, 947 (1999).
37. J.-S. Hong, *J. Electrochem. Soc.*, **145**, 1489 (1998).
38. L. D. Ellis, J. P. Allen, L. M. Thompson, J. E. Harlow, W. J. Stone, I. G. Hill, and J. R. Dahn, *J. Electrochem. Soc.*, **164**, A3518 (2017).
39. B. Rieger, S. V. Erhard, S. Kosch, M. Venator, A. Rheinfeld, and A. Jossen, *J. Electrochem. Soc.*, **163**, A3099 (2016).
40. S. V. Erhard, P. J. Osswald, J. Wilhelm, A. Rheinfeld, S. Kosch, and A. Jossen, *J. Electrochem. Soc.*, **162**, A2707 (2015).
41. S. V. Erhard et al., *J. Electrochem. Soc.*, **164**, A6324 (2017).
42. S. Kosch, Y. Zhao, J. Sturm, J. Schuster, G. Mulder, E. Ayerbe, and A. Jossen, *J. Electrochem. Soc.*, **165**, A2374 (2018).
43. J. Sturm, A. Rheinfeld, I. Zilberman, F. B. Spingler, S. Kosch, F. Frie, and A. Jossen, *Journal of Power Sources*, **412**, 204 (2019).
44. A. Rheinfeld, J. Sturm, A. Frank, S. Kosch, S. V. Erhard, and A. Jossen, *J. Electrochem. Soc.*, **167**, 013511 (2020).